

Comparison of Analytic and Algebraic Methods for Motion-Compensated Cone-Beam CT Reconstruction of the Thorax

Simon Rit, David Sarrut*, and Laurent Desbat

Abstract—Respiratory motion is a major concern in cone-beam (CB) computed tomography (CT) of the thorax. It causes artifacts such as blur, streaks, and bands, in particular when using slow-rotating scanners mounted on the gantry of linear accelerators. In this paper, we compare two approaches for motion-compensated CBCT reconstruction of the thorax. The first one is analytic; it is heuristically adapted from the method of Feldkamp, Davis, and Kress (FDK). The second one is algebraic: the system of linear equations is generated using a new algorithm for the projection of deformable volumes and solved using the Simultaneous Algebraic Reconstruction Technique (SART). For both methods, we propose to estimate the motion on patient data using a previously acquired 4-D CT image. The methods were tested on two digital and one mechanical motion-controlled phantoms and on a patient dataset. Our results indicate that the two methods correct most motion artifacts. However, the analytic method does not fully correct streaks and bands even if the motion is perfectly estimated due to the underlying approximation. In contrast, the algebraic method allows us full correction of respiratory-induced artifacts.

Index Terms—Image reconstruction, motion compensation, respiratory system, X-ray tomography.

I. INTRODUCTION

IN RADIOTHERAPY, 3-D cone-beam (CB) computed tomography (CT) images can now be acquired in the treatment room with a scanner mounted on the slow rotating gantry of the linear accelerator [1]. Unfortunately, like other motions and independently of the CT scanner used [2], respiratory motion causes significant artifacts in CT images of the thorax, such as blur, streaks and bands, which can lead to erroneous delineation of the tumor and organs [3]. Two main types of solutions have been proposed in CBCT to correct these artifacts prior to

Manuscript received July 05, 2008; revised October 16, 2008. This work was supported in part by Association Nationale de la Recherche Technique (ANRT) and in part by Elekta Oncology Systems. *Asterisk indicates corresponding author.*

S. Rit was with the University of Lyon—LIRIS—UMR CNRS 5205, Université Lumière Lyon 2, 69676 Bron, France. He is now with the Department of Radiation Oncology, The Netherlands Cancer Institute—Antoni van Leeuwenhoek Hospital, 1066 CX Amsterdam, The Netherlands.

*D. Sarrut is with the Radiotherapy Department, University of Lyon, Centre Léon Bérard, 69373 Lyon, France, and also with the CREATIS-LRMN—UMR CNRS 5220—INSERM U630, INSA—Bâtiment Blaise Pascal, 69621 Villeurbanne Cedex, France (e-mail: david.sarrut@creatis.insa-lyon.fr).

L. Desbat is with the TIMC-IMAG—UMR CNRS 5525, Grenoble University, UJF Medical Faculty, 38706 La Tronche, France.

Color versions of one or more of the figures in this paper are available online at <http://ieeexplore.ieee.org>.

Digital Object Identifier 10.1109/TMI.2008.2008962

or during reconstruction without requiring hardware evolution: respiration-correlated CT and motion-compensated CT.

Respiration-correlated CT, also known as retrospectively gated CT, uses a respiratory signal to sort CB projections according to their position in the respiratory cycle, which is supposed to be periodic during acquisition [4]–[7]. Each group of CB projections corresponds to a given phase of the cycle and is used to reconstruct the 3-D CT image of the phase, thus obtaining a 4-D CT image. The efficiency of respiration-correlated CT has been demonstrated and the method is currently used in stereotactic radiotherapy protocols [8]. However, as only a subset of the CB projections is used to reconstruct each 3-D CT image, the resulting image quality is low [9]. To improve image quality, more CB projections can be acquired by either slowing down the gantry [4] or doing several rotations [7], which significantly increases both the acquisition time and the X-ray dose delivered to the patient.

Motion-compensated CT uses a more precise motion model to compensate for respiratory motion during image reconstruction from all CB projections of the 3-D CT image at a reference instant. The technique is thus expected to provide the same image quality as in the static case when using the same acquisition protocol. Two problems have to be solved: motion estimation and motion-compensated reconstruction.

Motion estimation consists in estimating the trajectory in time of each physical point in the field-of-view. Trajectories are described by a motion model or 3-D+ t parameterization, such as B -splines or dense vector fields [10]. Ideally, the parameters of this motion model are estimated from available data, in this case from the 2-D+ t sequence of CB projections. But this problem is ill-posed and the lack of data must be compensated for. In angiography, Blondel *et al.* [11], [12] have proposed to base motion estimation on a preliminary 3-D geometric model of the coronary tree reconstructed from only two or three CB projections. Thoracic organs do not have sufficiently contrasted structures to allow such a geometric reconstruction and additional images are required. Zeng *et al.* [13], [14] have proposed to use a previously acquired breath-hold 3-D CT image. The objective function to minimize for motion estimation is then the difference between the measured CB projection and the projection of the CT image warped according to the current estimate of the respiratory motion. Instead of using only one image, other studies [15], [16] have estimated a model of the motion during one respiratory cycle using two prior 3-D images acquired at the extreme points of the cycle and registered it on the CB projections. This model has limited degrees-of-freedom and can be

more easily fitted to the CB projections. In summary, estimating the respiratory motion from CB projections is still a work in progress but these different studies suggest that it is feasible.

The second step to obtain the final 3-D CT image is to compensate for the estimated respiratory motion during reconstruction. This problem is still open and actively investigated. Currently proposed exact and analytic solutions are restricted to a limited class of deformations [17]–[19] which does not include the respiratory motion. Two solutions are therefore conceivable for analytic reconstruction: approximation of the respiratory motion by a deformation that can be exactly compensated for, or use of a heuristic solution [20]–[23].

Alternatively, an algebraic solution can be considered. It consists in iteratively solving a system of linear equations generated by taking into account the discrete nature of digital images. In the static case, the system is obtained by computing the intersection length of the straight acquisition line with basis functions, e.g., voxel indicator functions. In the dynamic case, the main difficulty is that basis functions should be deformed according to the motion before computing the intersection. If the deformation of the basis functions is ignored, the resulting image will be degraded by artifacts which are generally not acceptable except for some specific imaging modalities such as high contrast images, for example in angiography [11], [12]. In emission tomography, Reyes *et al.* [16] have proposed to use spheres as basis functions and to approximate their deformation by ellipsoids.

In this paper, we compare two approaches for motion-compensated CT reconstruction. The first one is analytic; it is heuristically adapted from the FDK method (Feldkamp, Davis, and Kress), similar to that described by Li *et al.* [21]. The second one is algebraic; the system of linear equations is generated using a new algorithm for the projection of deformable volumes and solved using the Simultaneous Algebraic Reconstruction Technique (SART). For both methods, the motion was estimated on patient data in two steps. First, the motion model of a respiratory cycle of the patient was estimated using a previously acquired 4-D CT image with deformable registration. Second, this model was registered spatially and temporally on the CB projections. The methods were tested on two digital and one mechanical motion-controlled phantoms and on a patient dataset.

II. NOTATIONS AND PRELIMINARY REMARKS

The objective of this work was to reconstruct the time-dependent function of linear attenuation coefficients, i.e., the 3-D+ t or 4-D CT image, defined by

$$\begin{aligned} f: \mathbb{R}^4 &\rightarrow \mathbb{R} \\ (\mathbf{x}, t) &\rightarrow f(\mathbf{x}, t) = f_t(\mathbf{x}) \end{aligned} \quad (1)$$

where $\mathbf{x} \in \mathbb{R}^3$ is the vector of the 3-D spatial coordinates in the Cartesian system and $t \in \mathbb{R}$ the time coordinate.

The geometry of the CB scanner used in this study is illustrated in Fig. 1. The trajectory of the source S describes a circle of radius $R \in \mathbb{R}$ in the plane $z = 0$ and centered around the origin O . The source position along the trajectory is defined by the angle $\beta \in [0, 2\pi)$ between the x axis and \vec{SO} : $(-R \cos \beta, -R \sin \beta, 0)$. The 2-D flat panel is perpendicular to \vec{SO} and provides CB projections P_β . A value $P_\beta(u, v)$ of a CB

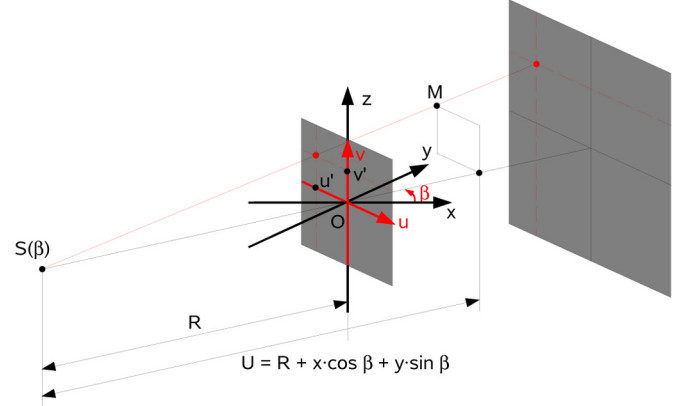


Fig. 1. Parameters of the CB geometry. We consider a virtual detector at the isocenter O , parallel to the real one and perpendicular to the source-isocenter line \vec{SO} . The system describes a circular rotation around the isocenter O parameterized by the angle β .

projection is identified by the coordinate pair $(u, v) \in \mathbb{R}^2$ on the virtual detector parallel to the real one and containing the origin O .

The X-ray transform links the function f to measurements acquired over one rotation following the relation:

$$P_\beta(u, v) = \int_{L_{\beta, u, v}} f(\mathbf{x}, t_\beta) d\mathbf{x} \quad (2)$$

where $L_{\beta, u, v}$ is the line passing through the X-ray source at position $S(\beta)$ and the point (u, v) of the virtual detector at the acquisition time t_β . β and t_β are linked by a bijective function as we acquire CB projections over one rotation only and without interruption of the rotation.

The correspondence between the position of a physical point (or particle [20]) at a reference time $t = 0$ and its position at any other time t during the acquisition is given by the 4-D motion model defined by

$$\begin{aligned} \Phi: \mathbb{R}^4 &\rightarrow \mathbb{R}^3 \\ (\mathbf{x}, t) &\rightarrow \Phi(\mathbf{x}, t) = \Phi_t(\mathbf{x}) \end{aligned} \quad (3)$$

where Φ_t is supposed to be a diffeomorphism on \mathbb{R}^3 (smooth bijection such that Φ_t^{-1} is smooth too).

As in [11] and [19], we assume that the linear attenuation coefficients at a given time are linked to the linear attenuation coefficients at the reference time by

$$f(\mathbf{x}, 0) = f(\Phi_t(\mathbf{x}), t). \quad (4)$$

In the following, this relation is used to compensate for the respiratory motion Φ during the reconstruction of the reference image f_0 . Any other CT image f_t can then be obtained by warping f_0 with Φ_t using (4).

III. METHODS

A. Analytic Reconstruction

As mentioned above, no exact solution has been proposed to compensate for the respiratory motion in analytic reconstruction algorithms. Our method is thus heuristic and derives from the

static reconstruction algorithm of Feldkamp, Davis and Kress (FDK) [24].

1) *Static Algorithm*: FDK approximate formula for the reconstruction of a stationary object from its CB projections is [24]

$$f_{\text{FDK}}(\mathbf{x}) = \int_0^{2\pi} \left(\frac{R}{U(\beta, \mathbf{x})} \right)^2 \tilde{P}'_{\beta}(u'(\beta, \mathbf{x}), v'(\beta, \mathbf{x})) d\beta \quad (5)$$

where

$$U(\beta, \mathbf{x}) = R + x \cos \beta + y \sin \beta$$

is the distance between the source $S(\beta)$ and the plane parallel to the flat panel containing the point M of coordinates $\mathbf{x} = (x, y, z)$ and

$$\begin{cases} u'(\beta, \mathbf{x}) = \frac{R(-x \sin \beta + y \cos \beta)}{U(\beta, \mathbf{x})} \\ v'(\beta, \mathbf{x}) = \frac{Rz}{U(\beta, \mathbf{x})} \end{cases}$$

are the coordinates on the virtual detector of the intersection point with the ray going through the source $S(\beta)$ and the point M . \tilde{P}'_{β} is obtained by successively weighting the projection P_{β} by

$$P'_{\beta}(u, v) = \frac{R}{\sqrt{R^2 + u^2 + v^2}} P_{\beta}(u, v) \quad (6)$$

and filtering the line of the weighted projection P'_{β} by

$$\tilde{P}'_{\beta}(u, v) = \int_{\mathbb{R}} \mathcal{F}_1 P'_{\beta}(\nu, v) e^{i2\pi\nu u} \frac{|\nu|}{2} d\nu \quad (7)$$

where $\mathcal{F}_1 P'_{\beta}$ is the 1-D Fourier transform of P'_{β} along its lines (first coordinate).

The heuristic mirroring proposed in [25] was also applied along the lines of the CB projections prior to the filter to correct for their truncation.

2) *Motion Compensation*: Deformations for which no exact compensation has been proposed, such as the one implied by respiratory motion, have been compensated heuristically in previous studies [20]–[23]. In these studies, the authors assume that a local application of global reconstruction algorithms is valid. The main modification implied by this assumption is a *voxel-specific* backprojection, i.e., the composition of the backprojection with the respiratory motion. In particular, Li *et al.* [21] proposed such compensation based on the FDK method, which yields the following reconstruction formula:

$$f_{\text{FDK}}(\mathbf{x}, 0) \simeq \int_0^{2\pi} \left(\frac{R}{U(\beta, \mathbf{y})} \right)^2 \times \tilde{P}'_{\beta}(u'(\beta, \mathbf{y}), v'(\beta, \mathbf{y})) d\beta \quad (8)$$

where $\mathbf{y} = \Phi_{t_{\beta}}(\mathbf{x})$. The weighting (6) and the filtering (7) are the same but the weighted backprojection (5) is evaluated at $\mathbf{y} = \Phi_{t_{\beta}}(\mathbf{x})$, the coordinates of M at time t_{β} (8). The resulting reconstruction algorithm consists in applying the following three steps for each CB projection P_{β} :

- 1) weight P_{β} to obtain P'_{β} (6);
- 2) filter P'_{β} to obtain \tilde{P}'_{β} (7);
- 3) weight and backproject \tilde{P}'_{β} along the \mathcal{C}^1 curves $\Phi_{t_{\beta}}^{-1}(L_{\beta, u, v})$ corresponding to the deformation of the

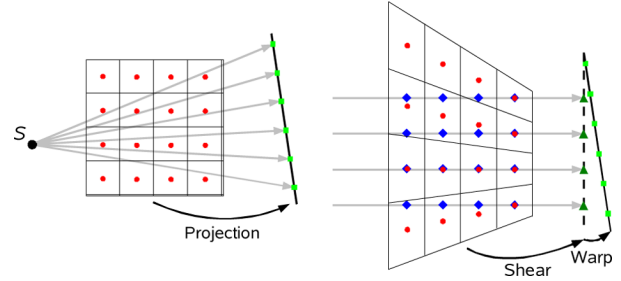


Fig. 2. Two-dimensional illustration of the shear-warp decomposition of the projection. Left: example of a projection of the CT volume (red circles) along X-rays (gray arrows) to obtain the CB projection (green squares). Right: corresponding shear-warp decomposition; first, the CT volume is *sheared* to align the samples intersected by a same ray in one direction of the orthogonal base of the CT volume (blue diamonds) and sum them in an intermediate image (dark green triangles); second, the intermediate image is *warped* with a 2-D affine transform to obtain the final CB projection.

straight acquisition line due to the respiratory motion between the acquisition instant t_{β} and the reference instant 0 (8).

B. Algebraic Reconstruction

Algebraic reconstruction methods belong to the wide category of discrete methods which take into account the discrete nature of the acquired and reconstructed data to pose and solve the inverse problem of CT reconstruction. We suppose therefore that f_0 can be decomposed as a linear combination of basis functions

$$f_0(\mathbf{x}) = \sum_{j=1}^N \mathbf{f}_j h_j(\mathbf{x}) \quad (9)$$

where $N \in \mathbb{N}$ is the number of voxels, $\mathbf{f} \in \mathbb{R}^N$ is the vector of the values of the CT image at the reference instant to be reconstructed and h_j are the basis functions. We chose as basis functions the voxel indicators, defined by

$$h_j(\mathbf{x}) = \begin{cases} 1, & \text{if } \mathbf{x} \text{ is in the } j\text{th voxel} \\ 0, & \text{else} \end{cases} \quad (10)$$

where $j \in \{1, \dots, N\}$ is the index of \mathbf{f} .

Let $\mathbf{b} \in \mathbb{R}^M$ be the vector of the $M \in \mathbb{N}$ measures, i.e., the pixel values of the set of CB projections. The technique is then twofold. First, the measures \mathbf{b} are linked to the CT image samples \mathbf{f} to be reconstructed. Second, the image \mathbf{f} is reconstructed by solving the system of linear equations using an algebraic method. We first briefly describe the static case and then discuss its adaptation to the dynamic case.

1) Static Algorithm:

a) *System of Linear Equations*: If the object is static during the acquisition, (2) becomes

$$\mathbf{b}_i = \int_{L_i} f(\mathbf{x}, t_{\beta}) d\mathbf{x} = \int_{L_i} f_0(\mathbf{x}) d\mathbf{x} \quad (11)$$

where $i \in \{1, \dots, M\}$ is the index of \mathbf{b} , corresponding to one measure acquired at position (β, u, v) at a given time t_{β} . Using the discrete representation of f_0 (9), we obtain

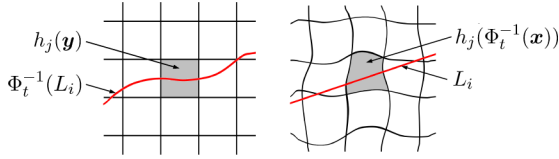


Fig. 3. Two-dimensional illustration of the two ways to compute the weights of \mathbf{A} in the dynamic case (18). Left: Intersection between the voxels $h_j(\mathbf{y})$ and the warped acquisition line $\Phi_t^{-1}(L_i)$ at the reference time 0 weighted by $\text{Jac}(\Phi_{t_\beta}(\mathbf{x}))$. Right: Intersection between the warped voxels $h_j(\Phi_t^{-1}(\mathbf{x}))$ and the straight acquisition line L_i at the acquisition time t_β .

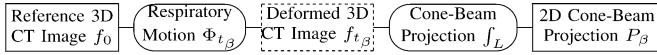


Fig. 4. Link between the reference CT image and a CB projection. The reference 3-D CT image f_0 is first warped to obtain the 3-D CT image f_{t_β} at the acquisition time t_β using the deformation Φ_{t_β} . It is then projected along acquisition lines L to obtain the 2-D CB projection P_β .

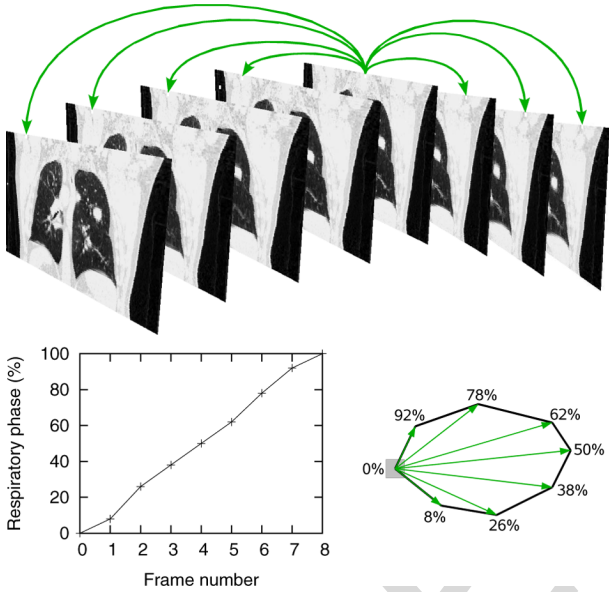


Fig. 5. Top: illustration of the vector fields estimated on a 4-D CT image between the reference 3-D CT image and each other image. They provide the displacement vector of each voxel of the reference 3-D CT image at different instants along the respiratory cycle. Bottom left: each 3-D CT image of the 4-D CT image is associated with one phase value of the respiratory cycle. Bottom right: example of the trajectory of one voxel of the reference 3-D CT image associated with the phase values.

$$\mathbf{b}_i = \int_{L_i} f_0(\mathbf{x}) d\mathbf{x} = \sum_{j=1}^N \left(\int_{L_i} h_j(\mathbf{x}) d\mathbf{x} \right) \mathbf{f}_j \quad (12)$$

where $\int_{L_i} h_j(\mathbf{x}) d\mathbf{x}$ is the length of the intersection between the j th voxel and the acquisition line L_i of the i th voxel. The following system of linear equations is obtained:

$$\mathbf{A}\mathbf{f} = \mathbf{b} \quad (13)$$

with

$$\mathbf{A}_{i,j} = \int_{L_i} h_j(\mathbf{x}) d\mathbf{x} \quad (14)$$

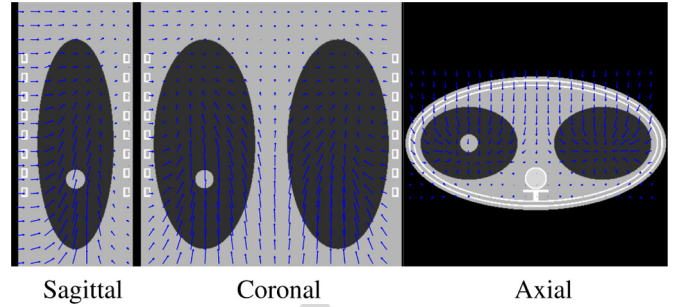


Fig. 6. Analytic digital phantom with analytic motion (Section IV-A1): slices at end-inhale (reference), with the computed motion vector field between end-inhale and end-exhale.

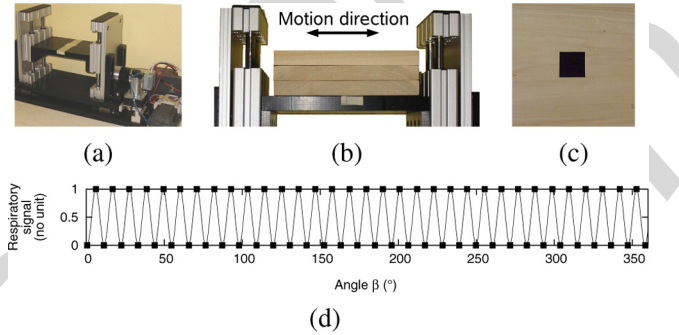


Fig. 7. Mechanical phantom (Section IV-A3) composed of (a) a mobile platform, on top of which is (b) a phantom composed of three wooden slabs with (c) a polyethylene cube inserted in the center of the middle slab. (d) Manually selected points (squares) with the fitted sinusoid (line) used as respiratory signal.

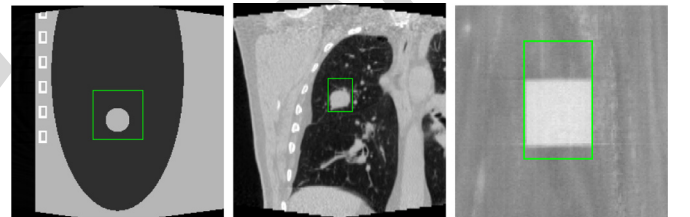


Fig. 8. Sagittal slices of the reference CT images of the three phantoms with the ROI used for the metrics.

b) Reconstruction Algorithm: Numerous algorithms can be used to solve this system of linear equations. We used the SART [26] which is a block version of the Algebraic Reconstruction Technique (ART) [27].

Following the notation in [28], we define

$$\begin{aligned} \mathbf{A}_{+,j} &= \sum_{k=1}^M \mathbf{A}_{k,j} \\ \mathbf{A}_{i,+} &= \sum_{k=1}^N \mathbf{A}_{i,k} \\ \bar{\mathbf{b}}_i(\mathbf{f}) &= \sum_{k=1}^N \mathbf{A}_{i,k} \mathbf{f}_k. \end{aligned}$$

The SART iteratively updates an initial guess (generally $\mathbf{f}_j^{(0)} = 0, \forall j \in \{1, \dots, N\}$) from *only one projection* P_β using the following correction formula:

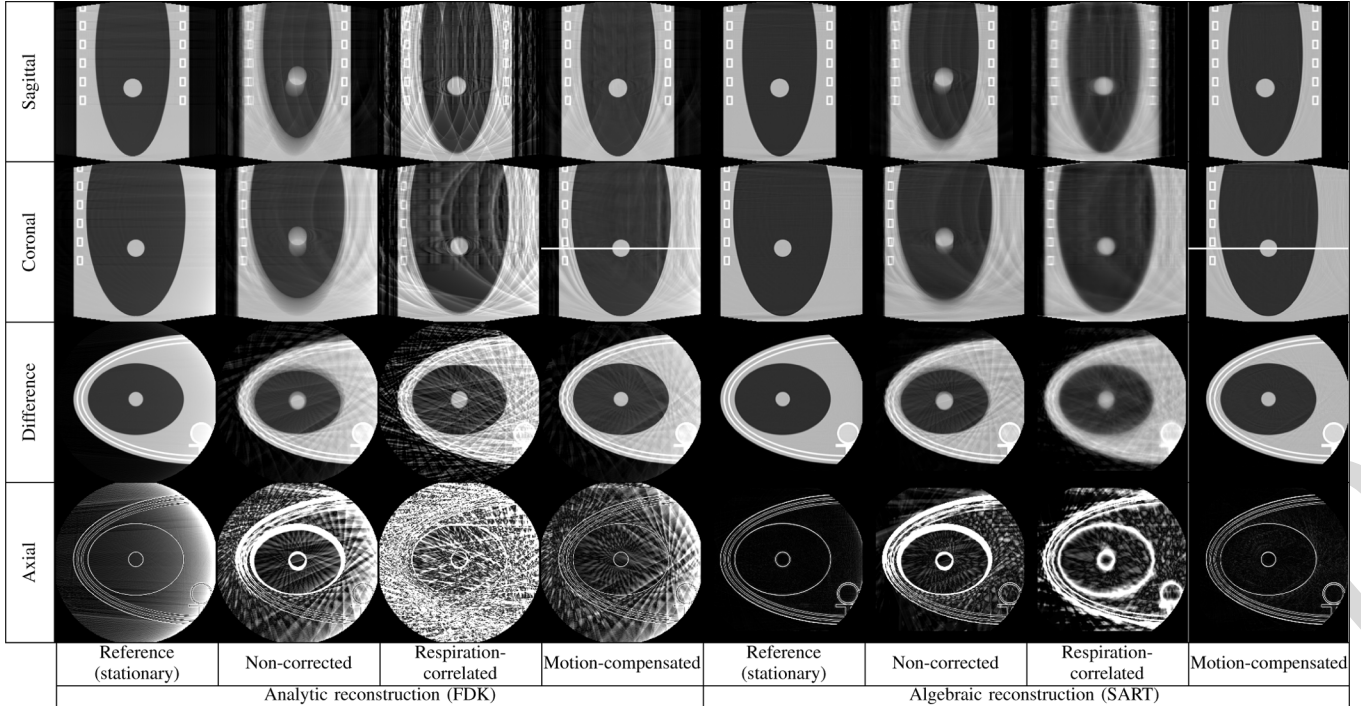


Fig. 9. Analytic digital phantom with analytic motion (Section IV-A1). First three rows: slices at the isocenter of the reconstructed CT images. Grey level window: $[0, 1.4]$. Last row: axial slice of the absolute difference between each reconstructed CT image and the reference CT scan. Grey level window: $[0, 0.2]$.

$$\mathbf{f}_j^{(m+1)} = \mathbf{f}_j^{(m)} + \frac{\lambda^{(m)}}{A_{+,j}} \sum_{\mathbf{b}_i \in P_\beta} \left(\frac{\mathbf{b}_i - \bar{\mathbf{b}}_i(\mathbf{f}^{(m)})}{A_{i,+}} \right) \mathbf{A}_{i,j} \quad (15)$$

where $m \in \mathbb{N}$ describes the step number. One iteration corresponds to one use of each CB projection, i.e., the application of (15) for all projections P_β . The correction applied by (15) from one projection P_β can be decomposed into the following steps.

- Step 1) Project the current volume $\mathbf{f}^{(m)}$ using the projection matrix \mathbf{A} to obtain an estimate $\bar{\mathbf{b}}(\mathbf{f}^{(m)})$ of the CB projection.
- Step 2) Compute the difference $\mathbf{b} - \bar{\mathbf{b}}(\mathbf{f}^{(m)})$ between the measured CB projection and the estimated CB projection, and normalize this difference by the sum $A_{i,+}$ of the weights along the ray of each pixel i of P_β .
- Step 3) Update the volume by backprojecting the normalized difference.

The quality of the output CT image then depends on the implementation of the reconstruction method which implies several choices for computer efficiency. It first depends on the projection ordering scheme, i.e., the order in which the CB projections P_β are used. We used the *weighted-distance scheme* [29]. It also depends on the projection method. Indeed, some authors have proposed more efficient projection methods in terms of computational time [30]–[32] instead of using the exact intersection between X-rays and voxel indicator functions [33]. We used the shear-warp algorithm [34] which is a two-step decomposition of the projection transform in a 3-D *shear* followed by a 2-D *warp* (Fig. 2). In this case, we modified the method as

proposed by [35] to apply the *warp* part to the measured CB projections instead of the intermediate image of the decomposition. This allows to reduce so-called edge and aliasing artifacts [36], [37] because warp resampling acts as a low pass filter on the measured CB projections. Step 2 of the SART algorithm is then performed in the intermediate space of the shear-warp decomposition. It finally depends on the backprojection method. For computer efficiency, we used a voxel-based backprojection (the one used in the FDK method without the weighting) instead of the transpose of the *shear-warp* projection.

The convergence of iterative methods has been studied in [38]. However, the convergence is obtained under the condition that the projector and the backprojector are dual operators. This is generally not fulfilled in our algorithm. Nevertheless, we apply only few iterations (three in our motion-compensated SART) which gives satisfactory results in our experiments.

Following Zhang *et al.* method [39], truncation artifacts were prevented during reconstruction by using a field-of-view including all voxels of the object reached at least once by the X-ray beam. Subsequently, only voxels reached by the X-ray beam in every direction β were visualized for the final result.

2) Motion Compensation:

a) *System of Linear Equations:* In the dynamic case, we made the assumption that $f(\Phi_t(\mathbf{x}), t) = f(\mathbf{x}, 0) = f_0(\mathbf{x})$ (4), or equivalently $f(\mathbf{x}, t) = f_0(\Phi_{t_\beta}^{-1}(\mathbf{x}))$. Thus, (11) is modified in

$$\mathbf{b}_i = \int_{L_i} f_0(\Phi_{t_\beta}^{-1}(\mathbf{x})) d\mathbf{x} \quad (16)$$

with β uniquely defined for a given i . Using the change of variable $\mathbf{y} = \Phi_{t_\beta}(\mathbf{x})$, it becomes

$$\mathbf{b}_i = \int_{\Phi_{t_\beta}^{-1}(L_i)} f_0(\mathbf{y}) \cdot \text{Jac}(\Phi_{t_\beta}(\mathbf{y})) d\mathbf{y} \quad (17)$$

where $\Phi_{t_\beta}^{-1}(L_i)$ is the \mathcal{C}^1 curve corresponding to the deformation of the straight acquisition line L_i due to the respiratory motion between the acquisition instant t_β and the reference instant 0, and $\text{Jac}(\Phi_{t_\beta}(\mathbf{y}))$ is the absolute value of the determinant of the Jacobian matrix of Φ_{t_β} at the point \mathbf{y} .

Using these two relations between the measured data \mathbf{b} and the attenuation function at the reference instant f_0 , we modify the coefficients of the system of linear (13) with

$$\begin{aligned} \mathbf{A}_{i,j} &= \int_{\Phi_{t_\beta}^{-1}(L_i)} h_j(\mathbf{y}) \cdot \text{Jac}(\Phi_{t_\beta}(\mathbf{y})) d\mathbf{y} \\ &= \int_{L_i} h_j(\Phi_{t_\beta}^{-1}(\mathbf{x})) d\mathbf{x}. \end{aligned} \quad (18)$$

The two possible strategies for computing the values of \mathbf{A} in the dynamic case are illustrated in Fig. 3. As already shown by other authors [11], [16], the exact intersections are difficult to compute in practice and some approximations have to be made. Fig. 4 summarizes the transforms involved in the process. An intuitive solution is to deform the reference 3-D CT image and to project the deformed image as in the static case [40]. However, explicitly computing the warped 3-D CT image requires an additional interpolation step which may alter the quality of the reconstructed image. In an earlier work [41], we proposed to avoid this additional interpolation by composing the two transforms. The respiratory displacement of each voxel of the reference CT image f_0 is composed with the shear transform of the shear-warp decomposition and the voxel intensity splatted at the new position using a linear kernel. To avoid aliasing artifacts, the splatting is done on a sheared 3-D image which is subsequently corrected by the sum of the splatting weights as proposed by [42].

b) Reconstruction Algorithm: The system of linear equations is similar to that described in the static case (13). Any iterative algorithm solving this kind of system could be used. We used the SART, as implemented in the static case. In particular, the backprojection was performed as in the motion-compensated analytic algorithm without the weighting.

C. Patient Motion Estimation

A proper estimation of the respiratory motion during the CB acquisition is required to apply the reconstruction methods to real data. We propose a new method which results from the combination of previous contributions.

The first step uses a 4-D CT image of the patient acquired on a conventional CT scanner for the planning of the radiotherapy treatment. The 4-D CT image was used to build a model of the patient respiratory cycle. The end-inhale 3-D CT image was chosen as the reference image f_0 . Dense motion vector fields were estimated between f_0 and all other 3-D CT images along the respiratory cycle using a deformable registration algorithm based on the Demons algorithm with a Gaussian regularization [43], [44]. We assumed that the resulting transformation was diffeomorphic although the Demons algorithm does not enforce it.

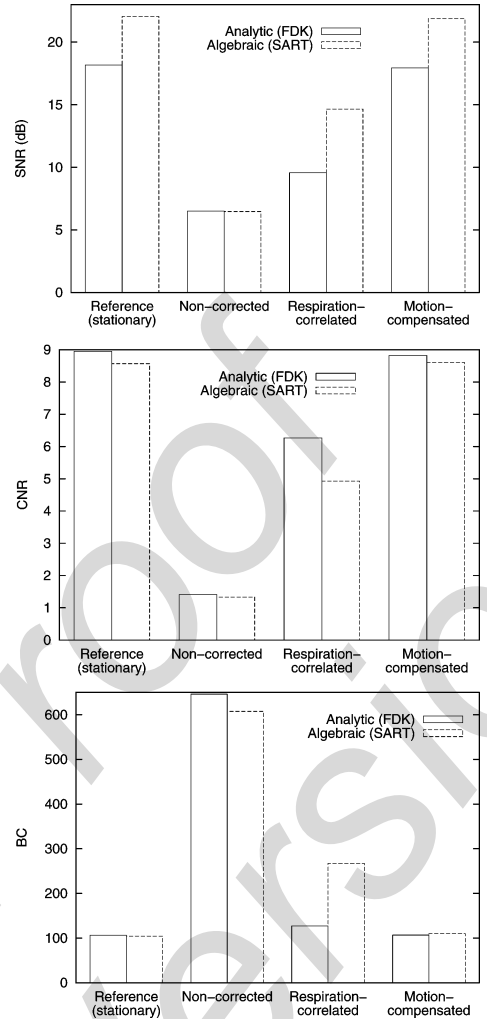


Fig. 10. Analytic digital phantom with analytic motion (Section IV-A1): quantitative analysis of reconstructed CT images (Fig. 9). The phantom was stationary for the reference image and dynamic for the other results.

A piecewise linear continuous trajectory corresponding to a full respiratory cycle is thus derived for each voxel, with differentiation of inhale and exhale to account for motion hysteresis [45] (Fig. 5).

The lung volume of each frame of the 4-D CT was digitally measured using a thresholding procedure combined with morphological operations [46]. The phase percentage of each frame along the respiratory cycle was deduced, 0% and 50% representing end-exhale and end-inhale phases, i.e., the minimum and the maximum lung volumes, respectively. Intermediate phase values were deduced based on lung volume variations (Fig. 5).

Sonke *et al.* [47] have observed a good reproducibility of the respiratory motion between the treatment fractions. Therefore, we assumed that the respiratory motion during the CB acquisition was similar to the motion model of the respiratory cycle built from the previous 4-D CT image. Estimating the respiratory motion consists then in registering the CB acquisition spatially and temporally to the model. Rigid spatial registration was performed between the blurred 3-D CT image of the model, obtained by averaging the previous 4-D CT image over time, and

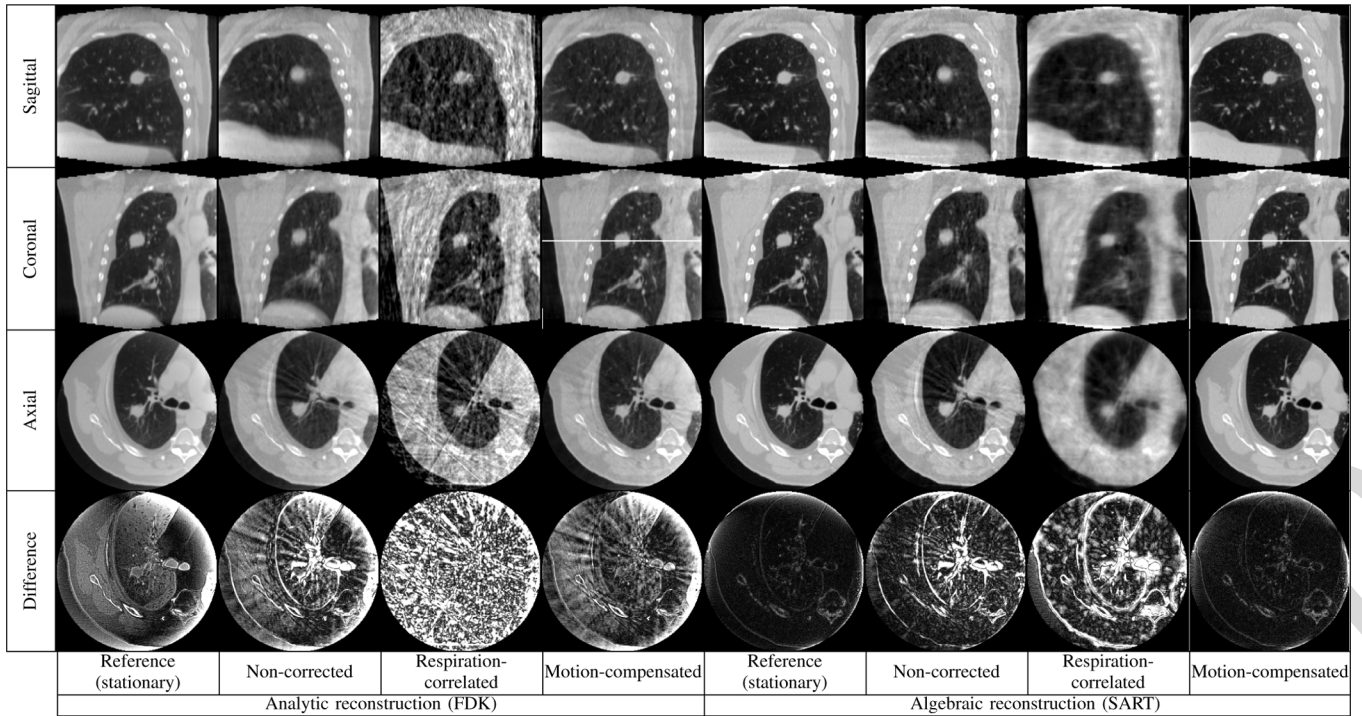


Fig. 11. Realistic digital phantom with realistic motion (Section IV-A2). First three rows: slices at the isocenter of the reconstructed CT images. Grey level window: $[0, 1.4]$. Last row: axial slice of the absolute difference between each reconstructed CT image and the reference CT scan. Grey level window: $[0, 0.2]$.

the blurred 3-D CBCT image obtained by reconstruction with the static FDK method (standard CBCT reconstruction without motion compensation) from all CB projections, as done by [48]. To account for the difference of noise between the two CT images, mutual information was used as a similarity measure [49].

The temporal registration between the sequence of CB projections and the model of the respiratory cycle was carried out using a respiratory signal. This signal was automatically extracted from the sequence of CB projections using motion analysis and signal processing as described in [50]. The phase of the respiratory signal was then processed to determine the percentage position along the respiratory cycle, end-exhale (0%) and end-inhale (50%) being positioned from peaks and valleys and intermediate phase values deduced linearly in time. Then, the resulting phase values were mapped to a temporal position in the motion model based on the phase value of each frame of the 4-D CT (Fig. 5).

The model of the respiratory cycle registered spatially and temporally at the acquisition time provides an estimate of the respiratory motion to be used when applying the proposed reconstruction methods to the patient dataset.

IV. EXPERIMENTS

A. Datasets

Experiments were conducted on four different sets of CB projections. Three phantoms (two digital and one mechanical, see descriptions below) with controllable motions were used to evaluate the reconstruction methods independently from the motion

estimation. One real patient dataset was used to test the combination of each reconstruction method with the motion estimation.

The geometry of the acquisition was the same for both the simulated and acquired CB projections: 640 CB projections acquired in 2 min over a full 360° rotation with a resolution of 512×512 pixels of size $0.52 \times 0.52 \text{ mm}^2$ at the isocenter and a source to isocenter distance $R = 1 \text{ m}$.

Patient motion, used for elaborating both the realistic digital phantom and the patient datasets, was estimated from a 4-D CT image acquired on a 16-slice helical CT scanner (Philips Brilliance CT Big Bore, Philips Medical System, Andover, MA) using a pressure belt to acquire the respiratory signal. Ten 3-D CT images regularly spaced along the respiratory cycle were reconstructed on a grid of $512 \times 512 \times 141$ voxels of size $0.98 \times 0.98 \times 2 \text{ mm}^3$. Two of the ten 3-D CT images were discarded because of residual motion artifacts, leaving eight 3-D CT images for motion estimation.

1) *Analytic Digital Phantom With Analytic Motion:* We created an analytic digital phantom of the thorax composed of several geometric objects (ellipsoids, cylinders, and boxes) at the two extreme positions of the respiratory cycle¹ (Fig. 6). Each object was defined by a set of parameters (center, radius, ...). End-exhale was a simplified version of the Forbild phantom² with an additional spherical tumor of 3 cm in diameter in the lower part of the right lung. End-inhale was obtained from end-exhale by manually choosing a new center and new dimensions for each geometric object in order to simulate a breathing motion. The

¹Detailed description available online: <http://www.creatis.insa-lyon.fr/rio/AnalyticThoraxPhantom>

²<http://www.imp.uni-erlangen.de/forbild/english/results/thorax/thorax.htm>

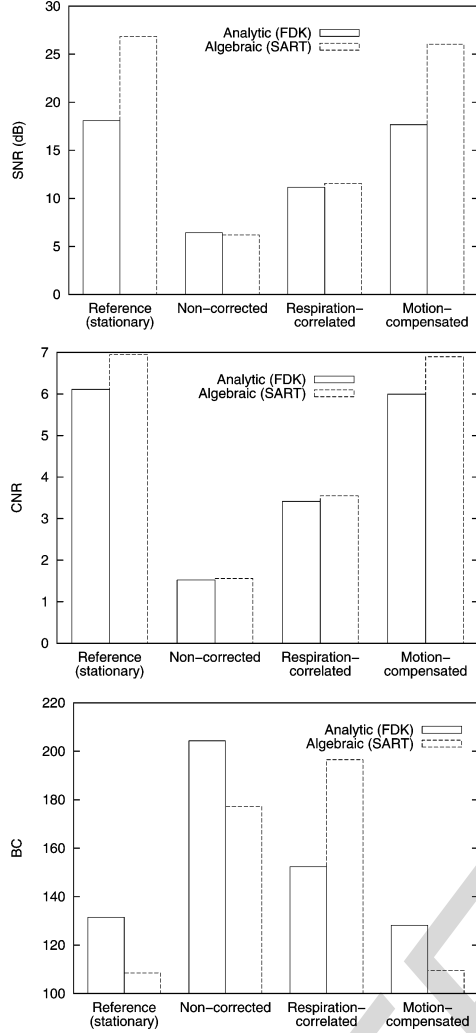


Fig. 12. Realistic digital phantom with realistic motion (Section IV-A2): quantitative analysis of the reconstructed CT images (Fig. 11). The phantom was stationary for the reference image and dynamic for the other results.

maximum displacement was 3.3 cm at the bottom of the lung ellipses and the maximum tumor displacement was 2.1 cm (70% of its diameter).

Between these two extreme states, the parameters of the geometric elements at intermediate states were derived continuously by linear interpolation of the parameters of each geometric element at extreme states with a respiratory signal between 0 (end-exhale) and 1 (end-inhale). For example, if p_e is the value at end-exhale of one of the parameters p and p_i its value at end-inhale, the value of p along time according to a respiratory signal $s(t)$ is $p(t) = s(t) \cdot p_i + (1 - s(t)) \cdot p_e$. The simulated regular respiratory signal s used as input was obtained from Lujan model [51]

$$s: \mathbb{R} \rightarrow \mathbb{R}$$

$$t \rightarrow s(t) = \cos^4\left(\frac{\pi t}{4}\right). \quad (19)$$

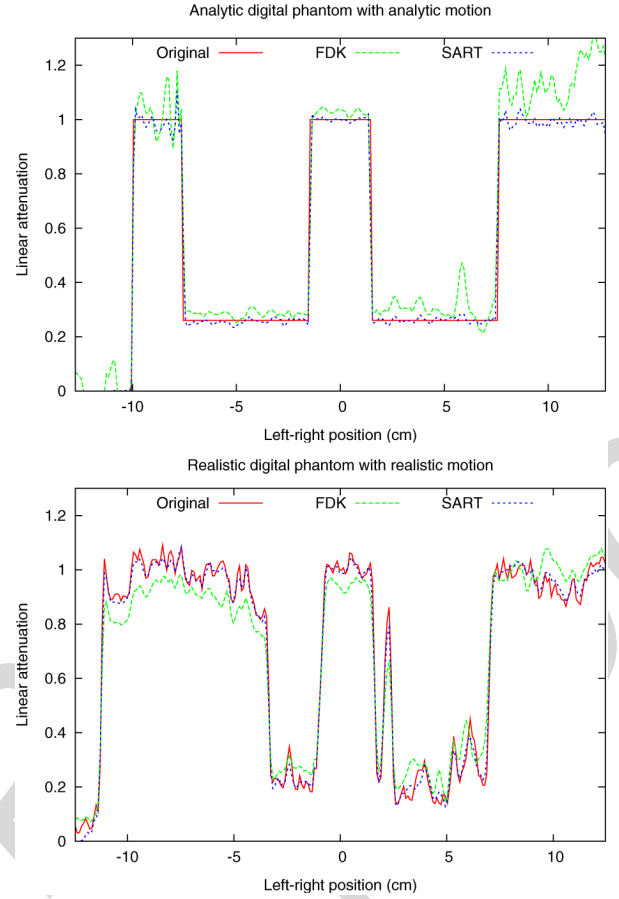


Fig. 13. Intensity profiles of the motion-compensated CBCT images of the digital phantoms in the left-right direction along the lines drawn on Figs. 9 and 11.

The analytic definition of any respiratory state allows then to compute independently the CB projection and the corresponding reference CT volume. This was done with the open-source software *Take*³.

The motion Φ of this phantom was estimated separately for the reconstruction only using end-inhale as the reference CT image. A dense vector field representing the deformation between end-inhale and end-exhale was computed using the previously described deformable registration method (Fig. 6). The deformation between end-inhale and an other time t was obtained by weighting the vector field between end-inhale and end-exhale with $1 - s(t)$.

2) *Realistic Digital Phantom With Realistic Motion*: A more realistic digital phantom was derived from the 4-D CT image of the patient used to estimate the motion from the sequence of CB projections of the patient (Section III-C, available online [52]). The respiratory motion at a given time t was simulated by considering each voxel trajectory as a piece-wise linear curve parameterized with the simulated respiratory signal s (19), as done in the real case with the measured respiratory signal (Fig. 5). CB projections were computed from the reference 3-D CT image and the motion model using the adequate projection matrix (18) to simulate the X-ray transform (2).

³<http://www.cvl.isy.liu.se/Research/Tomo/take/index.html>

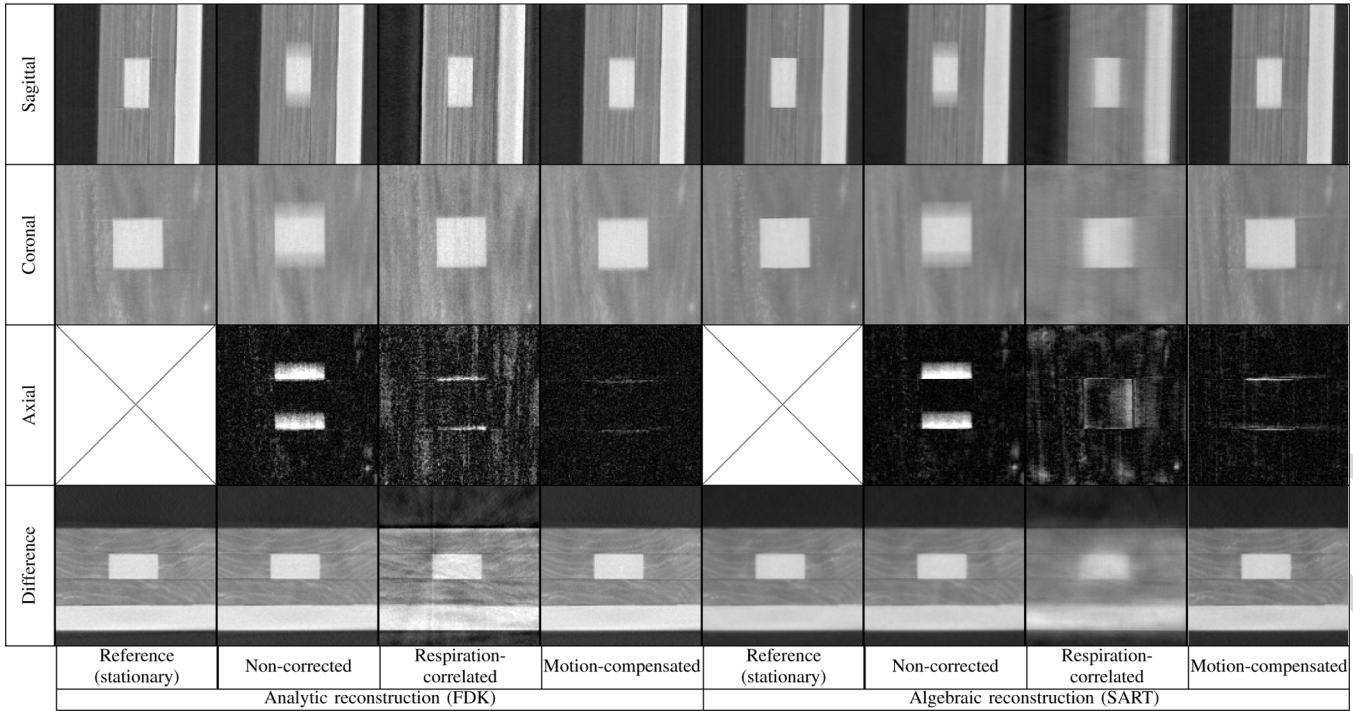


Fig. 14. Real data with a mechanical phantom (Section IV-A3). First, second and fourth rows: slices at the isocenter of the reconstructed CT images. Third row: coronal slice of the absolute difference between each reconstructed CT image and the reference CT scan. The images were cropped to a $128 \times 128 \text{ mm}^2$ size around the isocenter for a better visualization. An identical grey level window was used for all images.

3) *Real Data With a Mechanical Phantom*: A sequence of CB projections was acquired on the CBCT scanner of the Elekta Synergy system (Elekta Oncology Systems Ltd., West Sussex, U.K.) with a phantom placed on a mobile platform. The acquisition parameters were 120 kVp, 10 mA, and 10 ms. The motion of the platform was a sinusoidal translation in the cranio-caudal direction. The peak-to-peak amplitude was 14 mm and the period was 3.5 s. The phantom was composed of a stack of three $20 \times 20 \times 2 \text{ cm}^3$ slabs of wood ($\mu \simeq 0.4 \text{ g} \cdot \text{cm}^{-3}$) with a $4 \times 4 \times 2 \text{ cm}^3$ cube of polyethylene ($\mu = 0.98 \text{ g} \cdot \text{cm}^{-3}$) inserted in the center of the middle slab (Fig. 7).

The respiratory signal was estimated by automatically fitting a sinusoid on the points corresponding to the extreme positions of the platform. The temporal value of these points were selected manually on the sequence of CB projections [Fig. 7(d)]. The maximum translation was measured on the 3-D CT images acquired while the phantom was stationary at the two extreme positions of the platform. Finally, the motion model was obtained by weighting the maximum translation by the respiratory signal value at each acquisition time.

4) *Patient Data*: A sequence of CB projections was acquired on the patient for whom CB projections were simulated (Section IV-A2). The acquisition parameters were 120 kVp, 40 mA, and 25 ms. The diameter of the tumor was approximately 27 mm and its maximum displacement 11 mm.

B. Metrics

We used three metrics to evaluate quantitatively the reconstructed CT images of the phantoms. The first two metrics evaluated the noise induced by the motion and the reconstruction

technique, and the third one estimated the blur. These metrics were applied to a region of interest (ROI) containing the tumor (digital phantoms) or the insert (mechanical phantom) in every position of the phantoms (Fig. 8).

1) *Signal-to-Noise Ratio (SNR)*: The SNR is given by

$$\text{SNR}(\text{dB}) = 20 \log_{10} \frac{\text{RMS}(\text{signal})}{\text{RMS}(\text{noise})} \quad (20)$$

where RMS is the root mean square of voxel intensities, the signal is the expected CT image and the noise is the voxel-to-voxel difference between expected and reconstructed CT images.

2) *Contrast-to-Noise Ratio (CNR)*: The CNR is given by

$$\text{CNR} = \frac{|S_{\text{fg}} - S_{\text{bg}}|}{\sigma_{\text{bg}}} \quad (21)$$

where S_{fg} and S_{bg} are the mean pixel values in the foreground and background, respectively, and σ_{bg} the standard deviation of pixel values in the background. The foreground corresponds to the tumor region segmented in the ROI and the background to the rest of the ROI. The foreground of the ROI was segmented in reference CT images using a manually determined threshold.

3) *Blur Criterion (BC)*: The BC used in this study was proposed by Kriminski *et al.* [5] to quantify the blur independently from the noise. Measures with the BC have arbitrary units and are only comparable relatively to each other on images of a same object, higher values meaning higher blur. Thus, lower BC values mean better results.

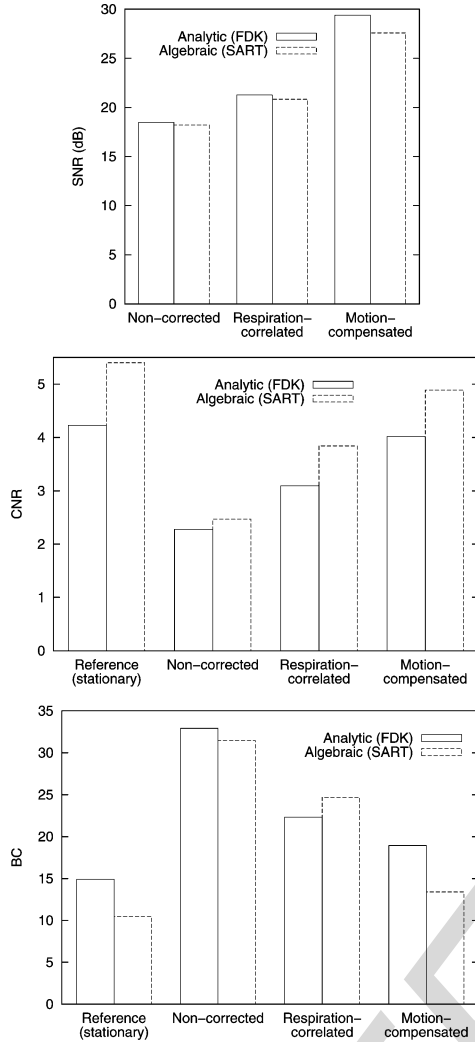


Fig. 15. Real data with a mechanical phantom (Section IV-A3): quantitative analysis of the reconstructed CT images (Fig. 14). The phantom was stationary for the reference image and dynamic for the other results. No reference value is given for the SNR as the reference CT image is used as a signal for SNR computation.

V. RESULTS

A. Reconstructed CT Images

Different CT images were reconstructed for each sequence of CB projections and each reconstruction technique (FDK and SART). The *noncorrected* CT images were reconstructed from all the CB projections using the static algorithm, which corresponds to the reconstruction when the motion is not taken into account. The *respiration-correlated* CT images were reconstructed from a subset of the CB projections using the same static algorithm. This subset was obtained by selecting, for each respiratory cycle, the CB projection closest to the reference position (end-inhale). Finally, the *motion-compensated* CT images were reconstructed from all the CB projections. For comparison, the reference CT images of the phantom were also reconstructed for the phantoms from the sequence of CB projections simulated or acquired with the phantom stationary at the reference position.

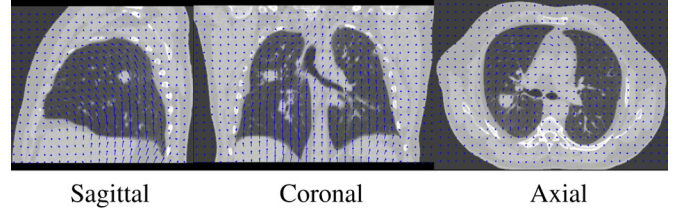


Fig. 16. Zoomed image of estimated motion vectors toward end-exhale superimposed on the slices of the reference CT image (end-inhale) of the 4-D CT image used for the realistic digital phantom and the patient data (Sections IV-A2 and IV-A4).

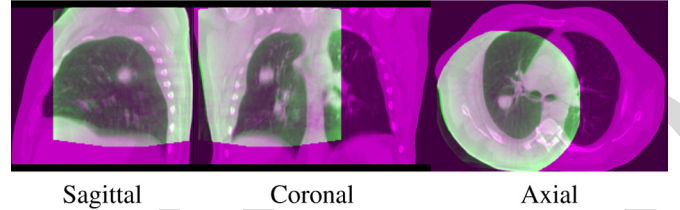


Fig. 17. Complementary color overlay of slices of the blurred 3-D CT image (green), reconstructed from all CB projections of the patient data (Section IV-A4), superimposed after rigid registration on the average 3-D CT image of the 4-D CT image (purple).

The resolution of the CT images was $256 \times 256 \times 256$ voxels of $1 \times 1 \times 1 \text{ mm}^3$ except for the realistic phantom for which it was identical to the resolution of the 3-D CT image used for simulation, i.e., $270 \times 270 \times 133$ voxels of $0.98 \times 0.98 \times 2 \text{ mm}^3$. For algebraic reconstruction, 3 iterations were performed for *static* and *motion-compensated* CT images [53] and 30 iterations for *respiration-correlated* CT images because the number of CB projections is lower.

The slices at the isocenter of the reconstructed CT images are given in Figs. 9, 11, 14, and 18. Profiles in the left-right direction through the tumor are given for the two motion-compensated CT images of the two digital phantoms in Fig. 13. The quantitative evaluation of phantom images is given in Figs. 10, 12, and 15.

B. Motion Estimation From Patient Data

The different components of the motion estimation of the patient were evaluated separately. The deformable registration, applied on the 4-D CT image acquired on a conventional CT scanner, was evaluated based on landmarks identified by medical experts [52], [54]. The mean/standard deviation of the target registration error was 1.2/0.4 mm, with a maximum of 2.6 mm. Fig. 16 illustrates one of the estimated vector fields. The respiratory signal was evaluated by comparing end-exhale and end-inhale temporal positions extracted (1) automatically from the respiratory signal based on changes of the derivative sign and (2) manually via a selection by an expert in the sequence of CB projections [55]. The mean absolute difference was 0.02 s. Finally, the precision of the rigid registration was visually assessed (Fig. 17).

VI. DISCUSSION AND CONCLUSION

Motion-compensated reconstruction allows to obtain CBCT images with a quality close to that obtained for the reconstruc-

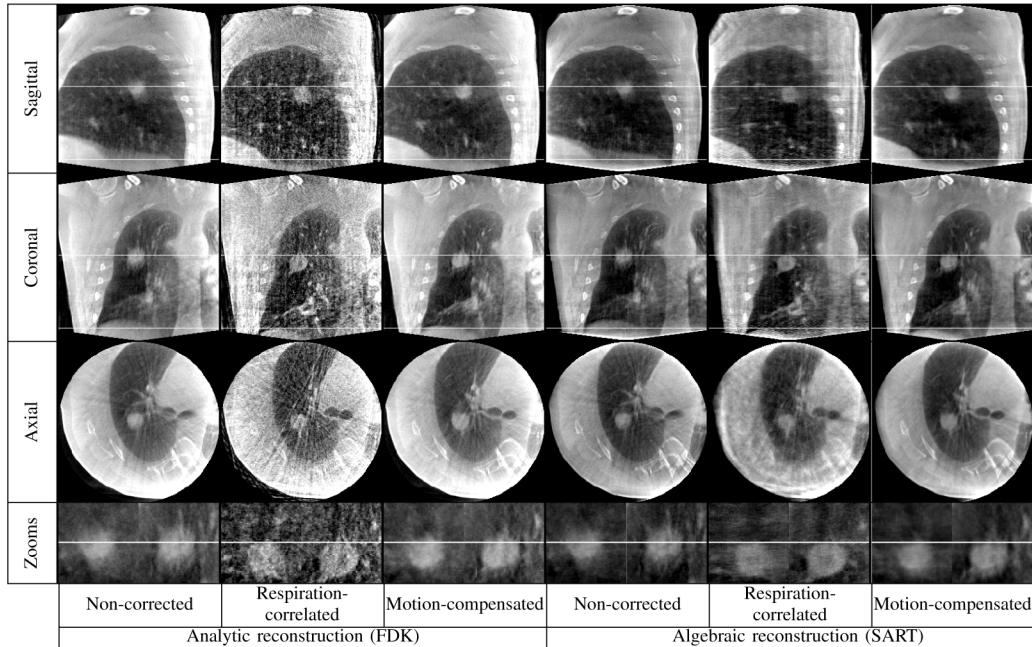


Fig. 18. Patient data (Section IV-A4): slices at the isocenter of the reconstructed CT images with zooms centered on the tumor on sagittal and coronal slices. An identical grey level window was used for all images.

tion of a stationary object using both the analytic (FDK) and the algebraic (SART) methods. The blur is almost fully eliminated and streaks and bands are reduced on the four datasets, both visually (Figs. 9, 11, 13, 14, and 18) and quantitatively on phantom data (Figs. 10, 12, and 15). These methods provide better results than respiration-correlated CBCT. Indeed, respiration-correlated CT involves the selection of only a subset of the CB projections, which causes artifacts due to missing data [4], [7]; these artifacts are mostly streaks and bands when using analytic reconstruction and blur when using algebraic reconstruction.

Numerical phantoms allow comparison between the analytic and the algebraic reconstruction independently from motion estimation because the motion model is then perfectly known. Quantitatively, the metric values are very close to the reference in both cases (Figs. 10 and 12). However, there is a perceptible visual difference between the two methods (Figs. 9, 11, and 13). The analytic reconstruction method, based on a heuristic, does not fully correct the streaks and bands, which is in accordance with Li *et al.* results [21]. Indeed, the analytic algorithm only compensates for the motion locally, in the regions where the motion takes place, while it is known that the motion of a contrasted object implies streak artifacts along the X-rays tangential to the object. These streaks can cross static regions where no compensation is applied. As a consequence, the streaks in motion-compensated CT images can be curved (Fig. 9). On the contrary, the algebraic reconstruction allows full correction of the motion artifacts. This is more visible on the difference images of axial slices where the remaining errors in algebraic reconstruction are mostly due to interpolation. Even though out of the scope of this paper, we note that the impact of truncation also varies with the method used: it causes more artifacts in analytic reconstruction

than in algebraic reconstruction (see reference images in Figs. 9 and 11).

The two reconstruction methods give promising results when applied to the two sequences of real CB projections (mechanical phantom and patient) acquired on the CB scanner but their comparative evaluation is more difficult than when using digital phantoms. First, the motion of the mechanical phantom was limited to a cranio-caudal translation which belongs to the category of deformations that can be exactly compensated [19]. Second, the estimation of patient motion was not precise because it relied on the hypotheses that the motion is regular and identical to the motion of the patient during the acquisition of the 4-D CT image on the conventional CT scanner. Therefore, we observe no visible differences between the two methods, unlike when using digital phantoms: the two motion compensated CT images of the mechanical phantom have a quality similarly close to the reference (Figs. 14 and 15) and both motion-compensated CT images of the patient partially correct the motion artifacts (Fig. 18).

The tissue deformations can imply variations of the linear attenuation of a physical point which were not taken into account in this study (4). For the three phantom datasets, this was because they were either not simulated (digital phantoms) or null (mechanical phantom animated by a rigid motion). However, for the patient dataset, the methods could be improved by characterizing the local variation of volume with the Jacobian of the deformation Φ as proposed by Rey *et al.* [56]: $dV_t \simeq \text{Jac}(\Phi_t) \cdot dV_0$. The local variation of volume can then be linked to the local variation of linear attenuation f by assuming that the linear attenuation is proportional to the mass density and by using the preservation of mass. Many other improvements could be made when operating on real data, such as scatter correction.

TABLE I
COMPUTATIONAL TIMES FOR THE RECONSTRUCTION OF THE IMAGES
OF THE MECHANICAL PHANTOM WITH AN IDENTICAL 256^3
VOXELS OF 1 mm^3 FIELD-OF-VIEW, I.E., NO CORRECTION
OF THE TRUNCATION IN ALGEBRAIC RECONSTRUCTION

Method	Reconstruction times	
	Analytic	Algebraic
Non-corrected	18 min	165 min
Motion-compensated	28 min	392 min

The computational time was not a major concern of this work but it is still interesting to observe the relative differences (Table I). With the analytic methods, motion-compensated reconstruction took 56% more time than uncompensated reconstruction; with the algebraic methods, the difference amounted to 138%. The two kinds of methods are not really comparable because a larger field of view is necessary to correct for the truncation when using algebraic reconstruction. But even when the same field-of-view was used, the motion-compensated reconstruction was 14 times longer with the algebraic method than with the analytic method. This is due to the algorithm complexity which is six times greater with algebraic reconstruction, due to the three projections and backprojections required per CB projection (one per iteration), than with analytic reconstruction which only involves one backprojection per CB projection. Moreover, the projection involves more computation than the backprojection.

Two cases can be sketched for clinical implementation. In the first case, the CBCT image is used just after the acquisition to estimate the patient's position. The estimation of the motion model from the 4-D CT image acquired on a conventional scanner could be done before the CB acquisition. As soon as an estimate of the spatial rigid registration is available, the motion-compensated CBCT image can be reconstructed on-the-fly using the analytic method to be available a few seconds after the end of the acquisition [57]. In the second case, the CBCT image is used after the delivery of the treatment fraction for adaptive radiation therapy [58]. Either of the proposed methods, analytic or algebraic, could then be used.

This study focused on the reconstruction aspects of motion-compensated CBCT. As estimating the respiratory motion is a prior to reconstruction, we proposed to prove the concepts on patient data by supposing that the respiratory motion was regular during the acquisition and similar to the one represented by the 4-D CT image acquired on a conventional scanner. Results obtained here on real patient data as well as another study on more patients [57] suggest that even a rough estimation can correct most motion artifacts but further validation based on more patient images is required to assess the robustness of the method to inaccuracies of the estimated motion. If necessary, the estimation could be improved with more sophisticated methods [14] which could use low quality reconstructed CBCT images to refine the motion estimation [59]. However, validation will be a major concern, as is the case with all nonrigid registration methods because no gold standard is available for patient data.

This study compared the quality of CBCT images reconstructed with analytic and algebraic methods. Motion-compensated algebraic reconstruction gave near perfect results when the motion was known whereas streak artifacts remained when

using analytic reconstruction (Figs. 9, 11, and 13). Future works will focus on motion estimation, which requires validation using an anthropomorphic phantom [60] and more patient images along with statistical analysis.

ACKNOWLEDGMENT

The authors would like to thank Prof. M. van Herk for critical reading and for permitting the use of the viewer developed at The Netherlands Cancer Institute.

REFERENCES

- [1] D. A. Jaffray, J. H. Siewerdsen, J. W. Wong, and A. A. Martinez, "Flat-panel cone-beam computed tomography for image-guided radiation therapy," *Int. J. Radiat. Oncol. Biol. Phys.*, vol. 53, no. 5, pp. 1337–1349, 2002.
- [2] C. J. Ritchie, J. D. Godwin, C. R. Crawford, W. Stanford, H. Anno, and Y. Kim, "Minimum scan speeds for suppression of motion artifacts in CT," *Radiology*, vol. 185, no. 1, pp. 37–42, 1992.
- [3] G. T. Y. Chen, J. H. Kung, and K. P. Beaudette, "Artifacts in computed tomography scanning of moving objects," *Semin. Radiat. Oncol.*, vol. 14, no. 1, pp. 19–26, 2004.
- [4] J.-J. Sonke, L. Zijp, P. Remeijer, and M. van Herk, "Respiratory correlated cone beam CT," *Med. Phys.*, vol. 32, no. 4, pp. 1176–1186, 2005.
- [5] S. Kriminski, M. Mitschke, S. Sorensen, N. M. Wink, P. E. Chow, S. Tenn, and T. D. Solberg, "Respiratory correlated cone-beam computed tomography on an isocentric C-arm," *Phys. Med. Biol.*, vol. 50, no. 22, pp. 5263–5280, 2005.
- [6] L. Dietrich, S. Jetter, T. Tücking, S. Nill, and U. Oelfke, "Linac-integrated 4-D cone beam CT: First experimental results," *Phys. Med. Biol.*, vol. 51, no. 11, pp. 2939–2952, 2006.
- [7] T. Li, L. Xing, P. Munro, C. McGuinness, M. Chao, Y. Yang, B. Loo, and A. Koong, "Four-dimensional cone-beam computed tomography using an on-board imager," *Med. Phys.*, vol. 33, no. 10, pp. 3825–3833, 2006.
- [8] M. van Herk, L. Zijp, P. Remeijer, J. Wolthaus, and J.-J. Sonke, "On-line 4-D cone beam CT for daily correction of lung tumour position during hypofractionated radiotherapy," in *Int. Conf. Use Comput. Radiation Therapy (ICCR)*, Toronto, ON, Canada, 2007.
- [9] S. Rit, D. Sarrut, and S. Miguet, "Gated cone-beam CT imaging of the thorax: A reconstruction study," in *SPIE Med. Imag.*, San Diego, CA, 2007, vol. 6510, p. 651022.
- [10] D. Sarrut, V. Boldea, S. Miguet, and C. Ginestet, "Simulation of four-dimensional CT images from deformable registration between inhale and exhale breath-hold CT scans," *Med. Phys.*, vol. 33, no. 3, pp. 605–617, 2006.
- [11] C. Blondel, R. Vaillant, G. Malandain, and N. Ayache, "3-D tomographic reconstruction of coronary arteries using a precomputed 4-D motion field," *Phys. Med. Biol.*, vol. 49, no. 11, pp. 2197–2208, 2004.
- [12] C. Blondel, G. Malandain, R. Vaillant, and N. Ayache, "Reconstruction of coronary arteries from a single rotational X-ray projection sequence," *IEEE Trans. Med. Imag.*, vol. 25, no. 5, pp. 653–663, May 2006.
- [13] R. Zeng, J. A. Fessler, and J. M. Balter, "Respiratory motion estimation from slowly rotating X-ray projections: Theory and simulation," *Med. Phys.*, vol. 32, no. 4, pp. 984–991, 2005.
- [14] R. Zeng, J. A. Fessler, and J. M. Balter, "Estimating 3-D respiratory motion from orbiting views by tomographic image registration," *IEEE Trans. Med. Imag.*, vol. 26, no. 2, pp. 153–163, Feb. 2007.
- [15] A. Schweikard, H. Shiomi, and J. Adler, "Respiration tracking in radio-surgery without fiducials," *Int. J. Med. Robot.*, vol. 1, no. 2, pp. 19–27, 2005.
- [16] M. Reyes, G. Malandain, P. M. Koulibaly, M. A. González-Ballester, and J. Darcourt, "Model-based respiratory motion compensation for emission tomography image reconstruction," *Phys. Med. Biol.*, vol. 52, no. 12, pp. 3579–3600, 2007.
- [17] C. R. Crawford, K. F. King, C. J. Ritchie, and J. D. Godwin, "Respiratory compensation in projection imaging using a magnification and displacement model," *IEEE Trans. Med. Imag.*, vol. 15, no. 3, pp. 327–332, Jun. 1996.
- [18] S. Roux, L. Desbat, A. Koenig, and P. Grangeat, "Exact reconstruction in 2-D dynamic CT: Compensation of time-dependent affine deformations," *Phys. Med. Biol.*, vol. 49, no. 11, pp. 2169–2182, 2004.

- [19] L. Desbat, S. Roux, and P. Grangeat, "Compensation of some time dependent deformations in tomography," *IEEE Trans. Med. Imag.*, vol. 26, no. 2, pp. 261–269, Feb. 2007.
- [20] P. Grangeat, A. Koenig, T. Rodet, and S. Bonnet, "Theoretical framework for a dynamic cone-beam reconstruction algorithm based on a dynamic particle model," *Phys. Med. Biol.*, vol. 47, no. 15, pp. 2611–2625, 2002.
- [21] T. Li, E. Schreibmann, Y. Yang, and L. Xing, "Motion correction for improved target localization with on-board cone-beam computed tomography," *Phys. Med. Biol.*, vol. 51, no. 2, pp. 253–267, 2006.
- [22] C. J. Ritchie, C. R. Crawford, J. D. Godwin, K. F. King, and Y. Kim, "Correction of computed tomography motion artifacts using pixel-specific back-projection," *IEEE Trans. Med. Imag.*, vol. 15, no. 3, pp. 333–342, Jun. 1996.
- [23] K. Taguchi and H. Kudo, "Motion compensated fan-beam reconstruction for nonrigid transformation," *IEEE Trans. Med. Imag.*, vol. 27, no. 7, pp. 907–917, Jul. 2008.
- [24] L. A. Feldkamp, L. C. Davis, and J. W. Kress, "Practical cone-beam algorithm," *J. Opt. Soc. Am. A*, vol. 1, no. 6, pp. 612–619, 1984.
- [25] B. Ohnesorge, T. Flohr, K. Schwarz, J. P. Heiken, and K. T. Bae, "Efficient correction for CT image artifacts caused by objects extending outside the scan field of view," *Med. Phys.*, vol. 27, no. 1, pp. 39–46, 2000.
- [26] A. H. Andersen and A. C. Kak, "Simultaneous algebraic reconstruction technique (SART): A superior implementation of the art algorithm," *Ultrason. Imag.*, vol. 6, no. 1, pp. 81–94, 1984.
- [27] R. Gordon, R. Bender, and G. T. Herman, "Algebraic reconstruction techniques (ART) for three-dimensional electron microscopy and X-ray photography," *J. Theor. Biol.*, vol. 29, no. 3, pp. 471–481, 1970.
- [28] M. Jiang and G. Wang, "Convergence of the simultaneous algebraic reconstruction technique (SART)," *IEEE Trans. Image Process.*, vol. 12, no. 8, pp. 957–961, Aug. 2003.
- [29] K. Mueller, R. Yagel, and J. F. Cornhill, "The weighted-distance scheme: A globally optimizing projection ordering method for ART," *IEEE Trans. Med. Imag.*, vol. 16, no. 2, pp. 223–230, Apr. 1997.
- [30] P. M. Joseph, "An improved algorithm for reprojecting rays through pixel images," *IEEE Trans. Med. Imag.*, vol. 1, no. 3, pp. 192–196, Nov. 1982.
- [31] B. De Man and S. Basu, "Distance-driven projection and backprojection in three dimensions," *Phys. Med. Biol.*, vol. 49, no. 11, pp. 2463–2475, 2004.
- [32] F. Xu and K. Mueller, "A comparative study of popular interpolation and integration methods for use in computed tomography," in *IEEE Int. Symp. Biomed. Imag. (ISBI)*, Apr. 2006, pp. 1252–1255.
- [33] R. L. Siddon, "Fast calculation of the exact radiological path for a three-dimensional CT array," *Med. Phys.*, vol. 12, no. 2, pp. 252–255, 1985.
- [34] P. G. Lacroute, "Fast volume rendering using a shear-warp factorization of the viewing transformation" Ph.D. dissertation, Stanford Univ., Stanford, CA, 1995 [Online]. Available: http://www-graphics.stanford.edu/papers/lacroute_thesis/
- [35] C. Riddell and Y. Trousset, "Rectification for cone-beam projection and backprojection," *IEEE Trans. Med. Imag.*, vol. 25, no. 7, pp. 950–962, Jul. 2006.
- [36] H. Kunze, K. Stierstorfer, and W. Härer, "Pre-processing of projections for iterative reconstruction," in *Fully 3-D Image Reconstruction Radiol. Nucl. Med. Conf.*, Salt Lake City, UT, 2005, pp. 84–87.
- [37] W. Zbijewski and F. J. Beekman, "Comparison of methods for suppressing edge and aliasing artefacts in iterative X-ray CT reconstruction," *Phys. Med. Biol.*, vol. 51, no. 7, pp. 1877–1889, 2006.
- [38] M. Jiang and G. Wang, "Convergence studies on iterative algorithms for image reconstruction," *IEEE Trans. Med. Imag.*, vol. 22, no. 5, pp. 569–579, May 2003.
- [39] B. Zhang and G. L. Zeng, "Two-dimensional iterative region-of-interest (ROI) reconstruction from truncated projection data," *Med. Phys.*, vol. 34, no. 3, pp. 935–944, 2007.
- [40] F. Lamare, T. Cresson, J. Savean, C. Cheze Le Rest, A. J. Reader, and D. Visvikis, "Respiratory motion correction for PET oncology applications using affine transformation of list mode data," *Phys. Med. Biol.*, vol. 52, no. 1, pp. 121–140, 2007.
- [41] S. Rit and D. Sarrut, "Cone-beam projection of a deformable volume for motion compensated algebraic reconstruction," in *Conf. Proc. IEEE Eng. Med. Biol. Soc.*, Lyon, France, 2007, vol. 2007, pp. 6544–6547.
- [42] G. Wolberg, *Digital Image Warping*. Los Alamitos, CA: IEEE Computer Soc. Press, 1990.
- [43] V. Boldea, D. Sarrut, and S. Clippe, "Lung deformation estimation with non-rigid registration for radiotherapy treatment," in *Medical Image Computing and Computer-Assisted Intervention (MICCAI)*, Montréal, QC, Canada, 2003, vol. 2878, pp. 770–777.
- [44] V. Boldea, G. C. Sharp, S. B. Jiang, and D. Sarrut, "4-D-CT lung motion estimation with deformable registration: Quantification of motion nonlinearity and hysteresis," *Med. Phys.*, vol. 35, no. 3, pp. 1008–1018, 2008.
- [45] Y. Seppenwoolde, H. Shirato, K. Kitamura, S. Shimizu, M. van Herk, J. V. Lebesque, and K. Miyasaka, "Precise and real-time measurement of 3-D tumor motion in lung due to breathing and heartbeat, measured during radiotherapy," *Int. J. Radiat. Oncol. Biol. Phys.*, vol. 53, no. 4, pp. 822–834, 2002.
- [46] V. Boldea, "Intégration de la Respiration en Radiothérapie : Apport du Recalage Déformable D'images" Ph.D. Dissertation, Univ. Lumière Lyon 2, Lyon, 2006 [Online]. Available: <http://liris.cnrs.fr/publis/?id=2959>
- [47] J.-J. Sonke, J. Lebesque, and M. van Herk, "Variability of four-dimensional computed tomography patient models," *Int. J. Radiat. Oncol. Biol. Phys.*, vol. 70, no. 2, pp. 590–598, 2008.
- [48] G. D. Hugo, J. Liang, J. Campbell, and D. Yan, "On-line target position localization in the presence of respiration: A comparison of two methods," *Int. J. Radiat. Oncol. Biol. Phys.*, vol. 69, no. 5, pp. 1634–1641, 2007.
- [49] J. Vandemeulebroucke, E. Vansteenkiste, and W. Philips, "A multimodal 2-D/3-D registration scheme for preterm brain images," in *Conf. Proc. IEEE Eng. Med. Biol. Soc.*, 2006, vol. 1, pp. 3341–3344.
- [50] S. Rit, D. Sarrut, and C. Ginestet, "Respiratory signal extraction for 4-D CT imaging of the thorax from cone-beam CT projections," in *Medical Image Computing and Computer-Assisted Intervention (MICCAI)*, Palm Springs, 2005, vol. 3749, pp. 556–563.
- [51] A. E. Lujan, E. W. Larsen, J. M. Balter, and R. K. Ten Haken, "A method for incorporating organ motion due to breathing into 3-D dose calculations," *Med. Phys.*, vol. 26, no. 5, pp. 715–720, 1999.
- [52] J. Vandemeulebroucke, D. Sarrut, and P. Clarysse, "Point-validated pixel-based breathing thorax model," in *Int. Conf. Use Computers Radiation Therapy (ICCR)*, Toronto, ON, Canada, 2007 [Online]. Available: <http://www.creatis.insa-lyon.fr/rio/popi-model>
- [53] K. Mueller, R. Yagel, and J. J. Wheller, "Anti-aliased three-dimensional cone-beam reconstruction of low-contrast objects with algebraic methods," *IEEE Trans. Med. Imag.*, vol. 18, no. 6, pp. 519–537, Jun. 1999.
- [54] D. Sarrut, B. Delhay, P.-F. Villard, V. Boldea, M. Beuve, and P. Clarysse, "A comparison framework for breathing motion estimation methods from 4-D imaging," *IEEE Trans. Med. Imag.*, vol. 26, no. 12, pp. 1636–1648, Dec. 2007.
- [55] S. Rit, "Prise en Compte du Mouvement Respiratoire Pour la Reconstruction D'images Tomodensitométriques" Ph.D. dissertation, Univ. Lumière Lyon 2, Lyon, France, 2007 [Online]. Available: <http://liris.cnrs.fr/publis/?id=3354>
- [56] D. Rey, G. Subsol, H. Delingette, and N. Ayache, "Automatic detection and segmentation of evolving processes in 3-D medical images: Application to multiple sclerosis," *Med. Image Anal.*, vol. 6, no. 2, pp. 163–179, 2002.
- [57] S. Rit, J. Wolthaus, M. van Herk, and J.-J. Sonke, "On-the-fly motion-compensated cone-beam CT using an a priori motion model," in *Medical Image Computing and Computer-Assisted Intervention (MICCAI)*, New York, 2008, vol. 5241, pp. 729–736.
- [58] D. Yan, F. Vicini, J. Wong, and A. Martinez, "Adaptive radiation therapy," *Phys. Med. Biol.*, vol. 42, no. 1, pp. 123–132, 1997.
- [59] T. Li, A. Koong, and L. Xing, "Enhanced 4-D cone-beam CT with inter-phase motion model," *Med. Phys.*, vol. 34, no. 9, pp. 3688–3695, 2007.
- [60] R. Lin, E. Wilson, J. Tang, D. Stoianovici, and K. Cleary, "A computer-controlled pump and realistic, anthropomorphic respiratory phantom for validating image-guided systems," in *SPIE Med. Imag.*, 2007, vol. 6510 [AUTHOR: PAGES?].

Comparison of Analytic and Algebraic Methods for Motion-Compensated Cone-Beam CT Reconstruction of the Thorax

Simon Rit, David Sarrut*, and Laurent Desbat

Abstract—Respiratory motion is a major concern in cone-beam (CB) computed tomography (CT) of the thorax. It causes artifacts such as blur, streaks, and bands, in particular when using slow-rotating scanners mounted on the gantry of linear accelerators. In this paper, we compare two approaches for motion-compensated CBCT reconstruction of the thorax. The first one is analytic; it is heuristically adapted from the method of Feldkamp, Davis, and Kress (FDK). The second one is algebraic: the system of linear equations is generated using a new algorithm for the projection of deformable volumes and solved using the Simultaneous Algebraic Reconstruction Technique (SART). For both methods, we propose to estimate the motion on patient data using a previously acquired 4-D CT image. The methods were tested on two digital and one mechanical motion-controlled phantoms and on a patient dataset. Our results indicate that the two methods correct most motion artifacts. However, the analytic method does not fully correct streaks and bands even if the motion is perfectly estimated due to the underlying approximation. In contrast, the algebraic method allows us full correction of respiratory-induced artifacts.

Index Terms—Image reconstruction, motion compensation, respiratory system, X-ray tomography.

I. INTRODUCTION

IN RADIOTHERAPY, 3-D cone-beam (CB) computed tomography (CT) images can now be acquired in the treatment room with a scanner mounted on the slow rotating gantry of the linear accelerator [1]. Unfortunately, like other motions and independently of the CT scanner used [2], respiratory motion causes significant artifacts in CT images of the thorax, such as blur, streaks and bands, which can lead to erroneous delineation of the tumor and organs [3]. Two main types of solutions have been proposed in CBCT to correct these artifacts prior to

Manuscript received July 05, 2008; revised October 16, 2008. This work was supported in part by Association Nationale de la Recherche Technique (ANRT) and in part by Elekta Oncology Systems. *Asterisk indicates corresponding author.*

S. Rit was with the University of Lyon—LIRIS—UMR CNRS 5205, Université Lumière Lyon 2, 69676 Bron, France. He is now with the Department of Radiation Oncology, The Netherlands Cancer Institute—Antoni van Leeuwenhoek Hospital, 1066 CX Amsterdam, The Netherlands.

*D. Sarrut is with the Radiotherapy Department, University of Lyon, Centre Léon Bérard, 69373 Lyon, France, and also with the CREATIS-LRMN—UMR CNRS 5220—INSERM U630, INSA—Bâtiment Blaise Pascal, 69621 Villeurbanne Cedex, France (e-mail: david.sarrut@creatis.insa-lyon.fr).

L. Desbat is with the TIMC-IMAG—UMR CNRS 5525, Grenoble University, UJF Medical Faculty, 38706 La Tronche, France.

Color versions of one or more of the figures in this paper are available online at <http://ieeexplore.ieee.org>.

Digital Object Identifier 10.1109/TMI.2008.2008962

or during reconstruction without requiring hardware evolution: respiration-correlated CT and motion-compensated CT.

Respiration-correlated CT, also known as retrospectively gated CT, uses a respiratory signal to sort CB projections according to their position in the respiratory cycle, which is supposed to be periodic during acquisition [4]–[7]. Each group of CB projections corresponds to a given phase of the cycle and is used to reconstruct the 3-D CT image of the phase, thus obtaining a 4-D CT image. The efficiency of respiration-correlated CT has been demonstrated and the method is currently used in stereotactic radiotherapy protocols [8]. However, as only a subset of the CB projections is used to reconstruct each 3-D CT image, the resulting image quality is low [9]. To improve image quality, more CB projections can be acquired by either slowing down the gantry [4] or doing several rotations [7], which significantly increases both the acquisition time and the X-ray dose delivered to the patient.

Motion-compensated CT uses a more precise motion model to compensate for respiratory motion during image reconstruction from all CB projections of the 3-D CT image at a reference instant. The technique is thus expected to provide the same image quality as in the static case when using the same acquisition protocol. Two problems have to be solved: motion estimation and motion-compensated reconstruction.

Motion estimation consists in estimating the trajectory in time of each physical point in the field-of-view. Trajectories are described by a motion model or 3-D+ t parameterization, such as B -splines or dense vector fields [10]. Ideally, the parameters of this motion model are estimated from available data, in this case from the 2-D+ t sequence of CB projections. But this problem is ill-posed and the lack of data must be compensated for. In angiography, Blondel *et al.* [11], [12] have proposed to base motion estimation on a preliminary 3-D geometric model of the coronary tree reconstructed from only two or three CB projections. Thoracic organs do not have sufficiently contrasted structures to allow such a geometric reconstruction and additional images are required. Zeng *et al.* [13], [14] have proposed to use a previously acquired breath-hold 3-D CT image. The objective function to minimize for motion estimation is then the difference between the measured CB projection and the projection of the CT image warped according to the current estimate of the respiratory motion. Instead of using only one image, other studies [15], [16] have estimated a model of the motion during one respiratory cycle using two prior 3-D images acquired at the extreme points of the cycle and registered it on the CB projections. This model has limited degrees-of-freedom and can be

more easily fitted to the CB projections. In summary, estimating the respiratory motion from CB projections is still a work in progress but these different studies suggest that it is feasible.

The second step to obtain the final 3-D CT image is to compensate for the estimated respiratory motion during reconstruction. This problem is still open and actively investigated. Currently proposed exact and analytic solutions are restricted to a limited class of deformations [17]–[19] which does not include the respiratory motion. Two solutions are therefore conceivable for analytic reconstruction: approximation of the respiratory motion by a deformation that can be exactly compensated for, or use of a heuristic solution [20]–[23].

Alternatively, an algebraic solution can be considered. It consists in iteratively solving a system of linear equations generated by taking into account the discrete nature of digital images. In the static case, the system is obtained by computing the intersection length of the straight acquisition line with basis functions, e.g., voxel indicator functions. In the dynamic case, the main difficulty is that basis functions should be deformed according to the motion before computing the intersection. If the deformation of the basis functions is ignored, the resulting image will be degraded by artifacts which are generally not acceptable except for some specific imaging modalities such as high contrast images, for example in angiography [11], [12]. In emission tomography, Reyes *et al.* [16] have proposed to use spheres as basis functions and to approximate their deformation by ellipsoids.

In this paper, we compare two approaches for motion-compensated CT reconstruction. The first one is analytic; it is heuristically adapted from the FDK method (Feldkamp, Davis, and Kress), similar to that described by Li *et al.* [21]. The second one is algebraic; the system of linear equations is generated using a new algorithm for the projection of deformable volumes and solved using the Simultaneous Algebraic Reconstruction Technique (SART). For both methods, the motion was estimated on patient data in two steps. First, the motion model of a respiratory cycle of the patient was estimated using a previously acquired 4-D CT image with deformable registration. Second, this model was registered spatially and temporally on the CB projections. The methods were tested on two digital and one mechanical motion-controlled phantoms and on a patient dataset.

II. NOTATIONS AND PRELIMINARY REMARKS

The objective of this work was to reconstruct the time-dependent function of linear attenuation coefficients, i.e., the 3-D+ t or 4-D CT image, defined by

$$\begin{aligned} f: \mathbb{R}^4 &\rightarrow \mathbb{R} \\ (\mathbf{x}, t) &\rightarrow f(\mathbf{x}, t) = f_t(\mathbf{x}) \end{aligned} \quad (1)$$

where $\mathbf{x} \in \mathbb{R}^3$ is the vector of the 3-D spatial coordinates in the Cartesian system and $t \in \mathbb{R}$ the time coordinate.

The geometry of the CB scanner used in this study is illustrated in Fig. 1. The trajectory of the source S describes a circle of radius $R \in \mathbb{R}$ in the plane $z = 0$ and centered around the origin O . The source position along the trajectory is defined by the angle $\beta \in [0, 2\pi)$ between the x axis and \vec{SO} : $(-R \cos \beta, -R \sin \beta, 0)$. The 2-D flat panel is perpendicular to \vec{SO} and provides CB projections P_β . A value $P_\beta(u, v)$ of a CB

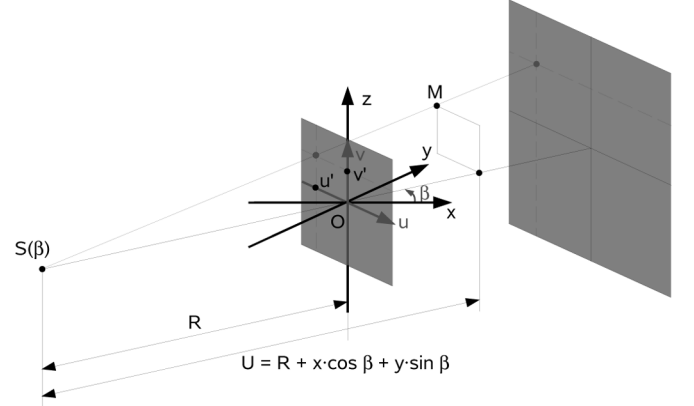


Fig. 1. Parameters of the CB geometry. We consider a virtual detector at the isocenter O , parallel to the real one and perpendicular to the source-isocenter line \vec{SO} . The system describes a circular rotation around the isocenter O parameterized by the angle β .

projection is identified by the coordinate pair $(u, v) \in \mathbb{R}^2$ on the virtual detector parallel to the real one and containing the origin O .

The X-ray transform links the function f to measurements acquired over one rotation following the relation:

$$P_\beta(u, v) = \int_{L_{\beta, u, v}} f(\mathbf{x}, t_\beta) d\mathbf{x} \quad (2)$$

where $L_{\beta, u, v}$ is the line passing through the X-ray source at position $S(\beta)$ and the point (u, v) of the virtual detector at the acquisition time t_β . β and t_β are linked by a bijective function as we acquire CB projections over one rotation only and without interruption of the rotation.

The correspondence between the position of a physical point (or particle [20]) at a reference time $t = 0$ and its position at any other time t during the acquisition is given by the 4-D motion model defined by

$$\begin{aligned} \Phi: \mathbb{R}^4 &\rightarrow \mathbb{R}^3 \\ (\mathbf{x}, t) &\rightarrow \Phi(\mathbf{x}, t) = \Phi_t(\mathbf{x}) \end{aligned} \quad (3)$$

where Φ_t is supposed to be a diffeomorphism on \mathbb{R}^3 (smooth bijection such that Φ_t^{-1} is smooth too).

As in [11] and [19], we assume that the linear attenuation coefficients at a given time are linked to the linear attenuation coefficients at the reference time by

$$f(\mathbf{x}, 0) = f(\Phi_t(\mathbf{x}), t). \quad (4)$$

In the following, this relation is used to compensate for the respiratory motion Φ during the reconstruction of the reference image f_0 . Any other CT image f_t can then be obtained by warping f_0 with Φ_t using (4).

III. METHODS

A. Analytic Reconstruction

As mentioned above, no exact solution has been proposed to compensate for the respiratory motion in analytic reconstruction algorithms. Our method is thus heuristic and derives from the

static reconstruction algorithm of Feldkamp, Davis and Kress (FDK) [24].

1) *Static Algorithm*: FDK approximate formula for the reconstruction of a stationary object from its CB projections is [24]

$$f_{\text{FDK}}(\mathbf{x}) = \int_0^{2\pi} \left(\frac{R}{U(\beta, \mathbf{x})} \right)^2 \tilde{P}'_{\beta}(u'(\beta, \mathbf{x}), v'(\beta, \mathbf{x})) d\beta \quad (5)$$

where

$$U(\beta, \mathbf{x}) = R + x \cos \beta + y \sin \beta$$

is the distance between the source $S(\beta)$ and the plane parallel to the flat panel containing the point M of coordinates $\mathbf{x} = (x, y, z)$ and

$$\begin{cases} u'(\beta, \mathbf{x}) = \frac{R(-x \sin \beta + y \cos \beta)}{U(\beta, \mathbf{x})} \\ v'(\beta, \mathbf{x}) = \frac{Rz}{U(\beta, \mathbf{x})} \end{cases}$$

are the coordinates on the virtual detector of the intersection point with the ray going through the source $S(\beta)$ and the point M . \tilde{P}'_{β} is obtained by successively weighting the projection P_{β} by

$$P'_{\beta}(u, v) = \frac{R}{\sqrt{R^2 + u^2 + v^2}} P_{\beta}(u, v) \quad (6)$$

and filtering the line of the weighted projection P'_{β} by

$$\tilde{P}'_{\beta}(u, v) = \int_{\mathbb{R}} \mathcal{F}_1 P'_{\beta}(\nu, v) e^{i2\pi\nu u} \frac{|\nu|}{2} d\nu \quad (7)$$

where $\mathcal{F}_1 P'_{\beta}$ is the 1-D Fourier transform of P'_{β} along its lines (first coordinate).

The heuristic mirroring proposed in [25] was also applied along the lines of the CB projections prior to the filter to correct for their truncation.

2) *Motion Compensation*: Deformations for which no exact compensation has been proposed, such as the one implied by respiratory motion, have been compensated heuristically in previous studies [20]–[23]. In these studies, the authors assume that a local application of global reconstruction algorithms is valid. The main modification implied by this assumption is a *voxel-specific* backprojection, i.e., the composition of the backprojection with the respiratory motion. In particular, Li *et al.* [21] proposed such compensation based on the FDK method, which yields the following reconstruction formula:

$$f_{\text{FDK}}(\mathbf{x}, 0) \simeq \int_0^{2\pi} \left(\frac{R}{U(\beta, \mathbf{y})} \right)^2 \times \tilde{P}'_{\beta}(u'(\beta, \mathbf{y}), v'(\beta, \mathbf{y})) d\beta \quad (8)$$

where $\mathbf{y} = \Phi_{t_{\beta}}(\mathbf{x})$. The weighting (6) and the filtering (7) are the same but the weighted backprojection (5) is evaluated at $\mathbf{y} = \Phi_{t_{\beta}}(\mathbf{x})$, the coordinates of M at time t_{β} (8). The resulting reconstruction algorithm consists in applying the following three steps for each CB projection P_{β} :

- 1) weight P_{β} to obtain P'_{β} (6);
- 2) filter P'_{β} to obtain \tilde{P}'_{β} (7);
- 3) weight and backproject \tilde{P}'_{β} along the \mathcal{C}^1 curves $\Phi_{t_{\beta}}^{-1}(L_{\beta, u, v})$ corresponding to the deformation of the

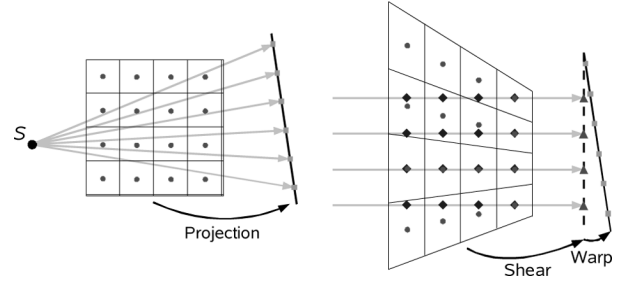


Fig. 2. Two-dimensional illustration of the shear-warp decomposition of the projection. Left: example of a projection of the CT volume (red circles) along X-rays (gray arrows) to obtain the CB projection (green squares). Right: corresponding shear-warp decomposition; first, the CT volume is *sheared* to align the samples intersected by a same ray in one direction of the orthogonal base of the CT volume (blue diamonds) and sum them in an intermediate image (dark green triangles); second, the intermediate image is *warped* with a 2-D affine transform to obtain the final CB projection.

straight acquisition line due to the respiratory motion between the acquisition instant t_{β} and the reference instant 0 (8).

B. Algebraic Reconstruction

Algebraic reconstruction methods belong to the wide category of discrete methods which take into account the discrete nature of the acquired and reconstructed data to pose and solve the inverse problem of CT reconstruction. We suppose therefore that f_0 can be decomposed as a linear combination of basis functions

$$f_0(\mathbf{x}) = \sum_{j=1}^N \mathbf{f}_j h_j(\mathbf{x}) \quad (9)$$

where $N \in \mathbb{N}$ is the number of voxels, $\mathbf{f} \in \mathbb{R}^N$ is the vector of the values of the CT image at the reference instant to be reconstructed and h_j are the basis functions. We chose as basis functions the voxel indicators, defined by

$$h_j(\mathbf{x}) = \begin{cases} 1, & \text{if } \mathbf{x} \text{ is in the } j\text{th voxel} \\ 0, & \text{else} \end{cases} \quad (10)$$

where $j \in \{1, \dots, N\}$ is the index of \mathbf{f} .

Let $\mathbf{b} \in \mathbb{R}^M$ be the vector of the $M \in \mathbb{N}$ measures, i.e., the pixel values of the set of CB projections. The technique is then twofold. First, the measures \mathbf{b} are linked to the CT image samples \mathbf{f} to be reconstructed. Second, the image \mathbf{f} is reconstructed by solving the system of linear equations using an algebraic method. We first briefly describe the static case and then discuss its adaptation to the dynamic case.

1) Static Algorithm:

a) *System of Linear Equations*: If the object is static during the acquisition, (2) becomes

$$\mathbf{b}_i = \int_{L_i} f(\mathbf{x}, t_{\beta}) d\mathbf{x} = \int_{L_i} f_0(\mathbf{x}) d\mathbf{x} \quad (11)$$

where $i \in \{1, \dots, M\}$ is the index of \mathbf{b} , corresponding to one measure acquired at position (β, u, v) at a given time t_{β} . Using the discrete representation of f_0 (9), we obtain

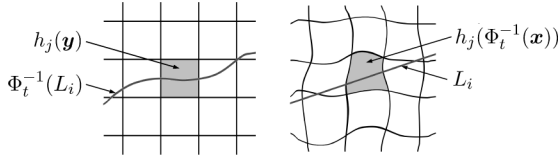


Fig. 3. Two-dimensional illustration of the two ways to compute the weights of \mathbf{A} in the dynamic case (18). Left: Intersection between the voxels $h_j(\mathbf{y})$ and the warped acquisition line $\Phi_t^{-1}(L_i)$ at the reference time 0 weighted by $\text{Jac}(\Phi_{t_\beta}(\mathbf{x}))$. Right: Intersection between the warped voxels $h_j(\Phi_t^{-1}(\mathbf{x}))$ and the straight acquisition line L_i at the acquisition time t_β .

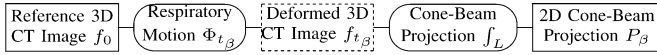


Fig. 4. Link between the reference CT image and a CB projection. The reference 3-D CT image f_0 is first warped to obtain the 3-D CT image f_{t_β} at the acquisition time t_β using the deformation Φ_{t_β} . It is then projected along acquisition lines L to obtain the 2-D CB projection P_β .

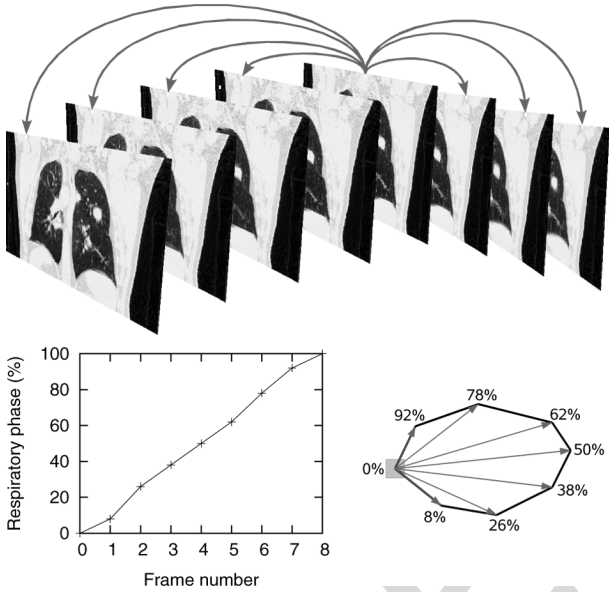


Fig. 5. Top: illustration of the vector fields estimated on a 4-D CT image between the reference 3-D CT image and each other image. They provide the displacement vector of each voxel of the reference 3-D CT image at different instants along the respiratory cycle. Bottom left: each 3-D CT image of the 4-D CT image is associated with one phase value of the respiratory cycle. Bottom right: example of the trajectory of one voxel of the reference 3-D CT image associated with the phase values.

$$\mathbf{b}_i = \int_{L_i} f_0(\mathbf{x}) d\mathbf{x} = \sum_{j=1}^N \left(\int_{L_i} h_j(\mathbf{x}) d\mathbf{x} \right) \mathbf{f}_j \quad (12)$$

where $\int_{L_i} h_j(\mathbf{x}) d\mathbf{x}$ is the length of the intersection between the j th voxel and the acquisition line L_i of the i th voxel. The following system of linear equations is obtained:

$$\mathbf{A}\mathbf{f} = \mathbf{b} \quad (13)$$

with

$$\mathbf{A}_{i,j} = \int_{L_i} h_j(\mathbf{x}) d\mathbf{x} \quad (14)$$

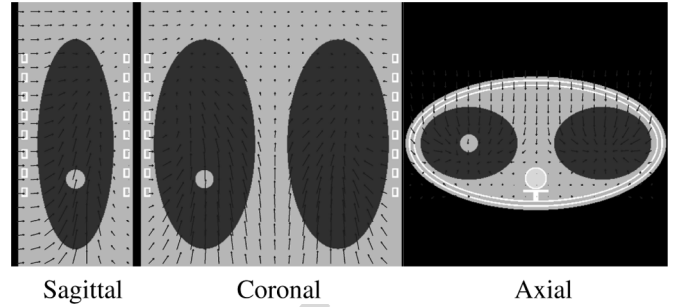


Fig. 6. Analytic digital phantom with analytic motion (Section IV-A1): slices at end-inhale (reference), with the computed motion vector field between end-inhale and end-exhale.

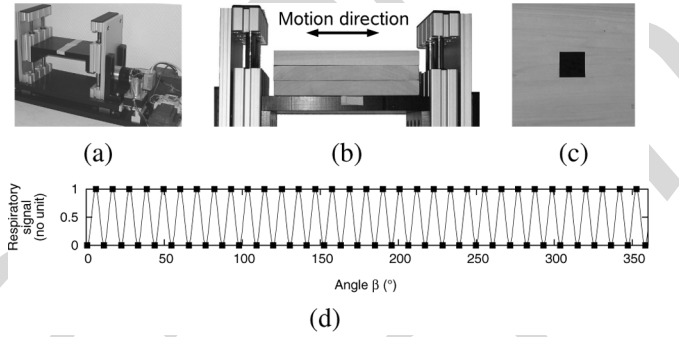


Fig. 7. Mechanical phantom (Section IV-A3) composed of (a) a mobile platform, on top of which is (b) a phantom composed of three wooden slabs with (c) a polyethylene cube inserted in the center of the middle slab. (d) Manually selected points (squares) with the fitted sinusoid (line) used as respiratory signal.

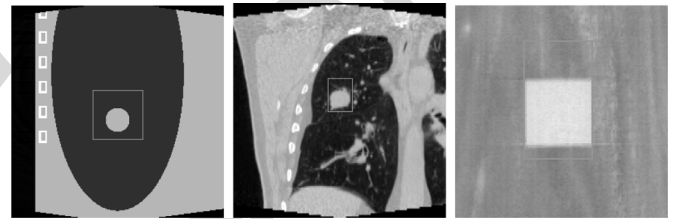


Fig. 8. Sagittal slices of the reference CT images of the three phantoms with the ROI used for the metrics.

b) Reconstruction Algorithm: Numerous algorithms can be used to solve this system of linear equations. We used the SART [26] which is a block version of the Algebraic Reconstruction Technique (ART) [27].

Following the notation in [28], we define

$$\begin{aligned} \mathbf{A}_{+,j} &= \sum_{k=1}^M \mathbf{A}_{k,j} \\ \mathbf{A}_{i,+} &= \sum_{k=1}^N \mathbf{A}_{i,k} \\ \bar{\mathbf{b}}_i(\mathbf{f}) &= \sum_{k=1}^N \mathbf{A}_{i,k} \mathbf{f}_k. \end{aligned}$$

The SART iteratively updates an initial guess (generally $\mathbf{f}_j^{(0)} = 0, \forall j \in \{1, \dots, N\}$) from *only one projection* P_β using the following correction formula:

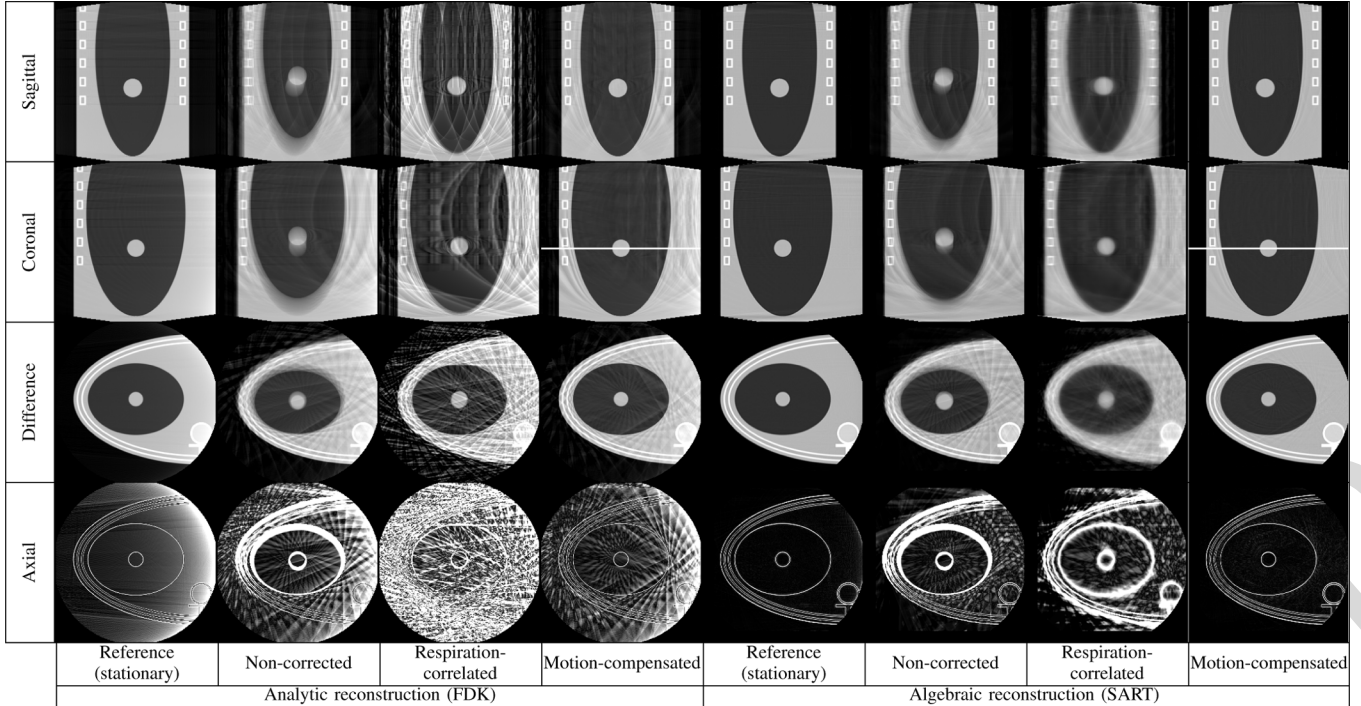


Fig. 9. Analytic digital phantom with analytic motion (Section IV-A1). First three rows: slices at the isocenter of the reconstructed CT images. Grey level window: $[0, 1.4]$. Last row: axial slice of the absolute difference between each reconstructed CT image and the reference CT scan. Grey level window: $[0, 0.2]$.

$$\mathbf{f}_j^{(m+1)} = \mathbf{f}_j^{(m)} + \frac{\lambda^{(m)}}{A_{+,j}} \sum_{\mathbf{b}_i \in P_\beta} \left(\frac{\mathbf{b}_i - \bar{\mathbf{b}}_i(\mathbf{f}^{(m)})}{A_{i,+}} \right) \mathbf{A}_{i,j} \quad (15)$$

where $m \in \mathbb{N}$ describes the step number. One iteration corresponds to one use of each CB projection, i.e., the application of (15) for all projections P_β . The correction applied by (15) from one projection P_β can be decomposed into the following steps.

- Step 1) Project the current volume $\mathbf{f}^{(m)}$ using the projection matrix \mathbf{A} to obtain an estimate $\bar{\mathbf{b}}(\mathbf{f}^{(m)})$ of the CB projection.
- Step 2) Compute the difference $\mathbf{b} - \bar{\mathbf{b}}(\mathbf{f}^{(m)})$ between the measured CB projection and the estimated CB projection, and normalize this difference by the sum $A_{i,+}$ of the weights along the ray of each pixel i of P_β .
- Step 3) Update the volume by backprojecting the normalized difference.

The quality of the output CT image then depends on the implementation of the reconstruction method which implies several choices for computer efficiency. It first depends on the projection ordering scheme, i.e., the order in which the CB projections P_β are used. We used the *weighted-distance scheme* [29]. It also depends on the projection method. Indeed, some authors have proposed more efficient projection methods in terms of computational time [30]–[32] instead of using the exact intersection between X-rays and voxel indicator functions [33]. We used the shear-warp algorithm [34] which is a two-step decomposition of the projection transform in a 3-D *shear* followed by a 2-D *warp* (Fig. 2). In this case, we modified the method as

proposed by [35] to apply the *warp* part to the measured CB projections instead of the intermediate image of the decomposition. This allows to reduce so-called edge and aliasing artifacts [36], [37] because warp resampling acts as a low pass filter on the measured CB projections. Step 2 of the SART algorithm is then performed in the intermediate space of the shear-warp decomposition. It finally depends on the backprojection method. For computer efficiency, we used a voxel-based backprojection (the one used in the FDK method without the weighting) instead of the transpose of the *shear-warp* projection.

The convergence of iterative methods has been studied in [38]. However, the convergence is obtained under the condition that the projector and the backprojector are dual operators. This is generally not fulfilled in our algorithm. Nevertheless, we apply only few iterations (three in our motion-compensated SART) which gives satisfactory results in our experiments.

Following Zhang *et al.* method [39], truncation artifacts were prevented during reconstruction by using a field-of-view including all voxels of the object reached at least once by the X-ray beam. Subsequently, only voxels reached by the X-ray beam in every direction β were visualized for the final result.

2) Motion Compensation:

a) *System of Linear Equations:* In the dynamic case, we made the assumption that $f(\Phi_t(\mathbf{x}), t) = f(\mathbf{x}, 0) = f_0(\mathbf{x})$ (4), or equivalently $f(\mathbf{x}, t) = f_0(\Phi_{t_\beta}^{-1}(\mathbf{x}))$. Thus, (11) is modified in

$$\mathbf{b}_i = \int_{L_i} f_0(\Phi_{t_\beta}^{-1}(\mathbf{x})) d\mathbf{x} \quad (16)$$

with β uniquely defined for a given i . Using the change of variable $\mathbf{y} = \Phi_{t_\beta}(\mathbf{x})$, it becomes

$$\mathbf{b}_i = \int_{\Phi_{t_\beta}^{-1}(L_i)} f_0(\mathbf{y}) \cdot \text{Jac}(\Phi_{t_\beta}(\mathbf{y})) d\mathbf{y} \quad (17)$$

where $\Phi_{t_\beta}^{-1}(L_i)$ is the \mathcal{C}^1 curve corresponding to the deformation of the straight acquisition line L_i due to the respiratory motion between the acquisition instant t_β and the reference instant 0, and $\text{Jac}(\Phi_{t_\beta}(\mathbf{y}))$ is the absolute value of the determinant of the Jacobian matrix of Φ_{t_β} at the point \mathbf{y} .

Using these two relations between the measured data \mathbf{b} and the attenuation function at the reference instant f_0 , we modify the coefficients of the system of linear (13) with

$$\begin{aligned} \mathbf{A}_{i,j} &= \int_{\Phi_{t_\beta}^{-1}(L_i)} h_j(\mathbf{y}) \cdot \text{Jac}(\Phi_{t_\beta}(\mathbf{y})) d\mathbf{y} \\ &= \int_{L_i} h_j(\Phi_{t_\beta}^{-1}(\mathbf{x})) d\mathbf{x}. \end{aligned} \quad (18)$$

The two possible strategies for computing the values of \mathbf{A} in the dynamic case are illustrated in Fig. 3. As already shown by other authors [11], [16], the exact intersections are difficult to compute in practice and some approximations have to be made. Fig. 4 summarizes the transforms involved in the process. An intuitive solution is to deform the reference 3-D CT image and to project the deformed image as in the static case [40]. However, explicitly computing the warped 3-D CT image requires an additional interpolation step which may alter the quality of the reconstructed image. In an earlier work [41], we proposed to avoid this additional interpolation by composing the two transforms. The respiratory displacement of each voxel of the reference CT image f_0 is composed with the shear transform of the shear-warp decomposition and the voxel intensity splatted at the new position using a linear kernel. To avoid aliasing artifacts, the splatting is done on a sheared 3-D image which is subsequently corrected by the sum of the splatting weights as proposed by [42].

b) Reconstruction Algorithm: The system of linear equations is similar to that described in the static case (13). Any iterative algorithm solving this kind of system could be used. We used the SART, as implemented in the static case. In particular, the backprojection was performed as in the motion-compensated analytic algorithm without the weighting.

C. Patient Motion Estimation

A proper estimation of the respiratory motion during the CB acquisition is required to apply the reconstruction methods to real data. We propose a new method which results from the combination of previous contributions.

The first step uses a 4-D CT image of the patient acquired on a conventional CT scanner for the planning of the radiotherapy treatment. The 4-D CT image was used to build a model of the patient respiratory cycle. The end-inhale 3-D CT image was chosen as the reference image f_0 . Dense motion vector fields were estimated between f_0 and all other 3-D CT images along the respiratory cycle using a deformable registration algorithm based on the Demons algorithm with a Gaussian regularization [43], [44]. We assumed that the resulting transformation was diffeomorphic although the Demons algorithm does not enforce it.

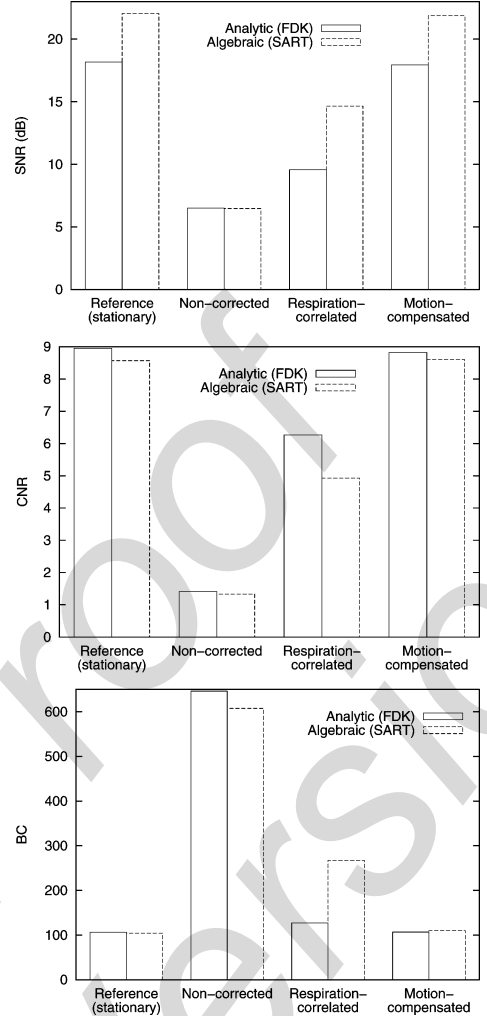


Fig. 10. Analytic digital phantom with analytic motion (Section IV-A1): quantitative analysis of reconstructed CT images (Fig. 9). The phantom was stationary for the reference image and dynamic for the other results.

A piecewise linear continuous trajectory corresponding to a full respiratory cycle is thus derived for each voxel, with differentiation of inhale and exhale to account for motion hysteresis [45] (Fig. 5).

The lung volume of each frame of the 4-D CT was digitally measured using a thresholding procedure combined with morphological operations [46]. The phase percentage of each frame along the respiratory cycle was deduced, 0% and 50% representing end-exhale and end-inhale phases, i.e., the minimum and the maximum lung volumes, respectively. Intermediate phase values were deduced based on lung volume variations (Fig. 5).

Sonke *et al.* [47] have observed a good reproducibility of the respiratory motion between the treatment fractions. Therefore, we assumed that the respiratory motion during the CB acquisition was similar to the motion model of the respiratory cycle built from the previous 4-D CT image. Estimating the respiratory motion consists then in registering the CB acquisition spatially and temporally to the model. Rigid spatial registration was performed between the blurred 3-D CT image of the model, obtained by averaging the previous 4-D CT image over time, and

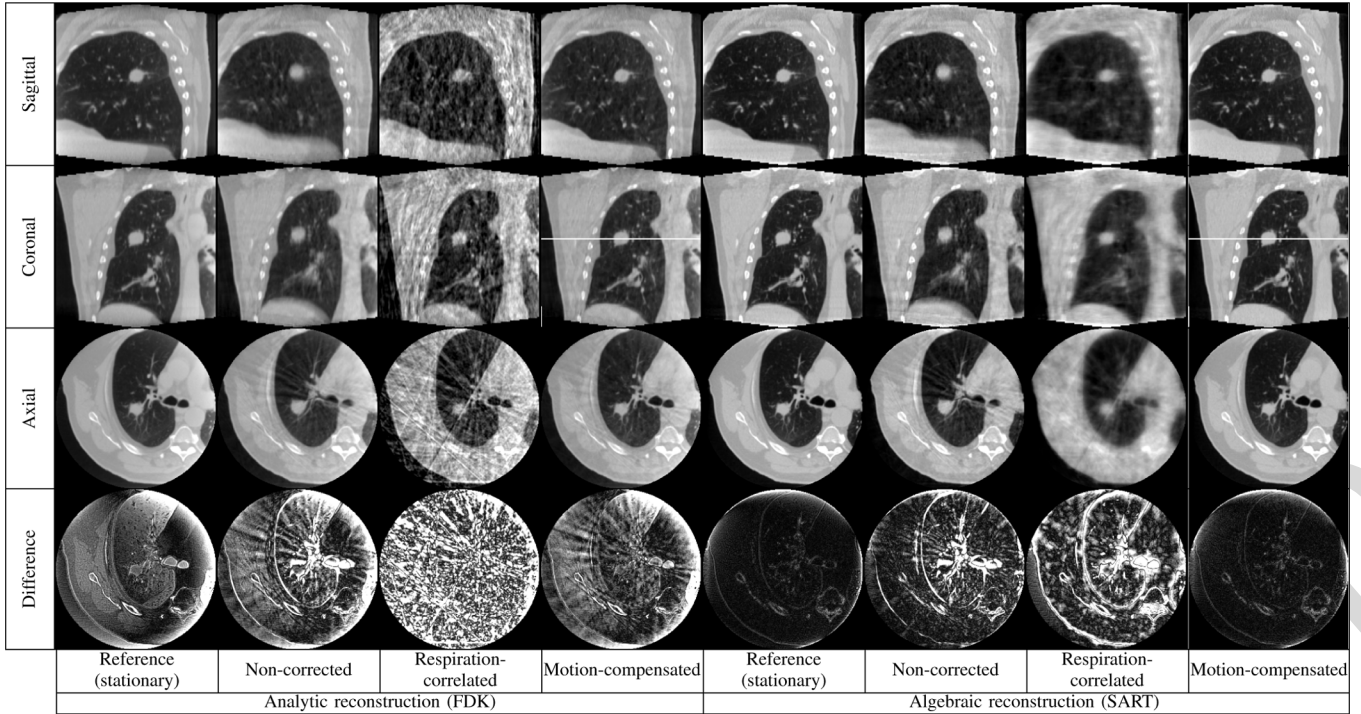


Fig. 11. Realistic digital phantom with realistic motion (Section IV-A2). First three rows: slices at the isocenter of the reconstructed CT images. Grey level window: $[0, 1.4]$. Last row: axial slice of the absolute difference between each reconstructed CT image and the reference CT scan. Grey level window: $[0, 0.2]$.

the blurred 3-D CBCT image obtained by reconstruction with the static FDK method (standard CBCT reconstruction without motion compensation) from all CB projections, as done by [48]. To account for the difference of noise between the two CT images, mutual information was used as a similarity measure [49].

The temporal registration between the sequence of CB projections and the model of the respiratory cycle was carried out using a respiratory signal. This signal was automatically extracted from the sequence of CB projections using motion analysis and signal processing as described in [50]. The phase of the respiratory signal was then processed to determine the percentage position along the respiratory cycle, end-exhale (0%) and end-inhale (50%) being positioned from peaks and valleys and intermediate phase values deduced linearly in time. Then, the resulting phase values were mapped to a temporal position in the motion model based on the phase value of each frame of the 4-D CT (Fig. 5).

The model of the respiratory cycle registered spatially and temporally at the acquisition time provides an estimate of the respiratory motion to be used when applying the proposed reconstruction methods to the patient dataset.

IV. EXPERIMENTS

A. Datasets

Experiments were conducted on four different sets of CB projections. Three phantoms (two digital and one mechanical, see descriptions below) with controllable motions were used to evaluate the reconstruction methods independently from the motion

estimation. One real patient dataset was used to test the combination of each reconstruction method with the motion estimation.

The geometry of the acquisition was the same for both the simulated and acquired CB projections: 640 CB projections acquired in 2 min over a full 360° rotation with a resolution of 512×512 pixels of size $0.52 \times 0.52 \text{ mm}^2$ at the isocenter and a source to isocenter distance $R = 1 \text{ m}$.

Patient motion, used for elaborating both the realistic digital phantom and the patient datasets, was estimated from a 4-D CT image acquired on a 16-slice helical CT scanner (Philips Brilliance CT Big Bore, Philips Medical System, Andover, MA) using a pressure belt to acquire the respiratory signal. Ten 3-D CT images regularly spaced along the respiratory cycle were reconstructed on a grid of $512 \times 512 \times 141$ voxels of size $0.98 \times 0.98 \times 2 \text{ mm}^3$. Two of the ten 3-D CT images were discarded because of residual motion artifacts, leaving eight 3-D CT images for motion estimation.

1) *Analytic Digital Phantom With Analytic Motion:* We created an analytic digital phantom of the thorax composed of several geometric objects (ellipsoids, cylinders, and boxes) at the two extreme positions of the respiratory cycle¹ (Fig. 6). Each object was defined by a set of parameters (center, radius, ...). End-exhale was a simplified version of the Forbild phantom² with an additional spherical tumor of 3 cm in diameter in the lower part of the right lung. End-inhale was obtained from end-exhale by manually choosing a new center and new dimensions for each geometric object in order to simulate a breathing motion. The

¹Detailed description available online: <http://www.creatis.insa-lyon.fr/rio/AnalyticThoraxPhantom>

²<http://www.imp.uni-erlangen.de/forbild/english/results/thorax/thorax.htm>

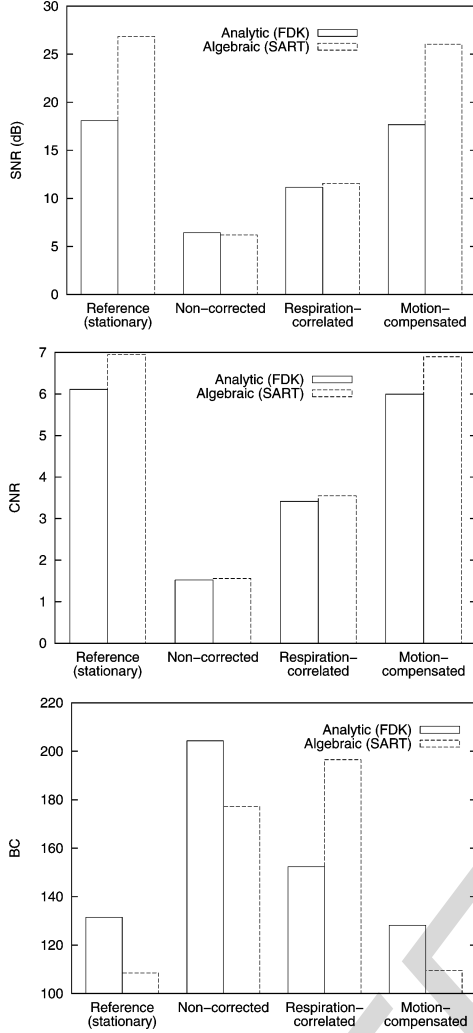


Fig. 12. Realistic digital phantom with realistic motion (Section IV-A2): quantitative analysis of the reconstructed CT images (Fig. 11). The phantom was stationary for the reference image and dynamic for the other results.

maximum displacement was 3.3 cm at the bottom of the lung ellipses and the maximum tumor displacement was 2.1 cm (70% of its diameter).

Between these two extreme states, the parameters of the geometric elements at intermediate states were derived continuously by linear interpolation of the parameters of each geometric element at extreme states with a respiratory signal between 0 (end-exhale) and 1 (end-inhale). For example, if p_e is the value at end-exhale of one of the parameters p and p_i its value at end-inhale, the value of p along time according to a respiratory signal $s(t)$ is $p(t) = s(t) \cdot p_i + (1 - s(t)) \cdot p_e$. The simulated regular respiratory signal s used as input was obtained from Lujan model [51]

$$s: \mathbb{R} \rightarrow \mathbb{R}$$

$$t \rightarrow s(t) = \cos^4\left(\frac{\pi t}{4}\right). \quad (19)$$

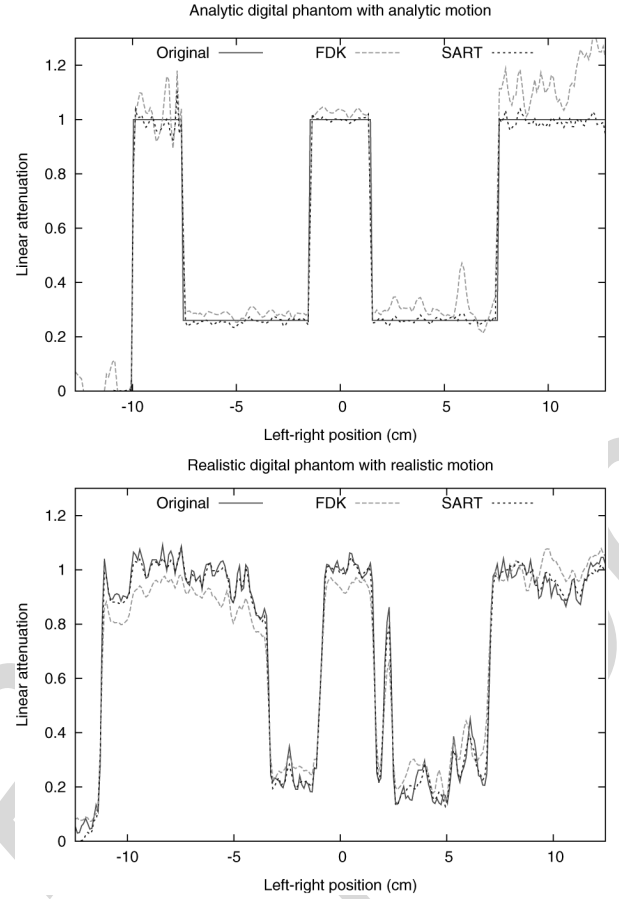


Fig. 13. Intensity profiles of the motion-compensated CBCT images of the digital phantoms in the left-right direction along the lines drawn on Figs. 9 and 11.

The analytic definition of any respiratory state allows then to compute independently the CB projection and the corresponding reference CT volume. This was done with the open-source software *Take*³.

The motion Φ of this phantom was estimated separately for the reconstruction only using end-inhale as the reference CT image. A dense vector field representing the deformation between end-inhale and end-exhale was computed using the previously described deformable registration method (Fig. 6). The deformation between end-inhale and an other time t was obtained by weighting the vector field between end-inhale and end-exhale with $1 - s(t)$.

2) *Realistic Digital Phantom With Realistic Motion*: A more realistic digital phantom was derived from the 4-D CT image of the patient used to estimate the motion from the sequence of CB projections of the patient (Section III-C, available online [52]). The respiratory motion at a given time t was simulated by considering each voxel trajectory as a piece-wise linear curve parameterized with the simulated respiratory signal s (19), as done in the real case with the measured respiratory signal (Fig. 5). CB projections were computed from the reference 3-D CT image and the motion model using the adequate projection matrix (18) to simulate the X-ray transform (2).

³<http://www.cvl.isy.liu.se/Research/Tomo/take/index.html>

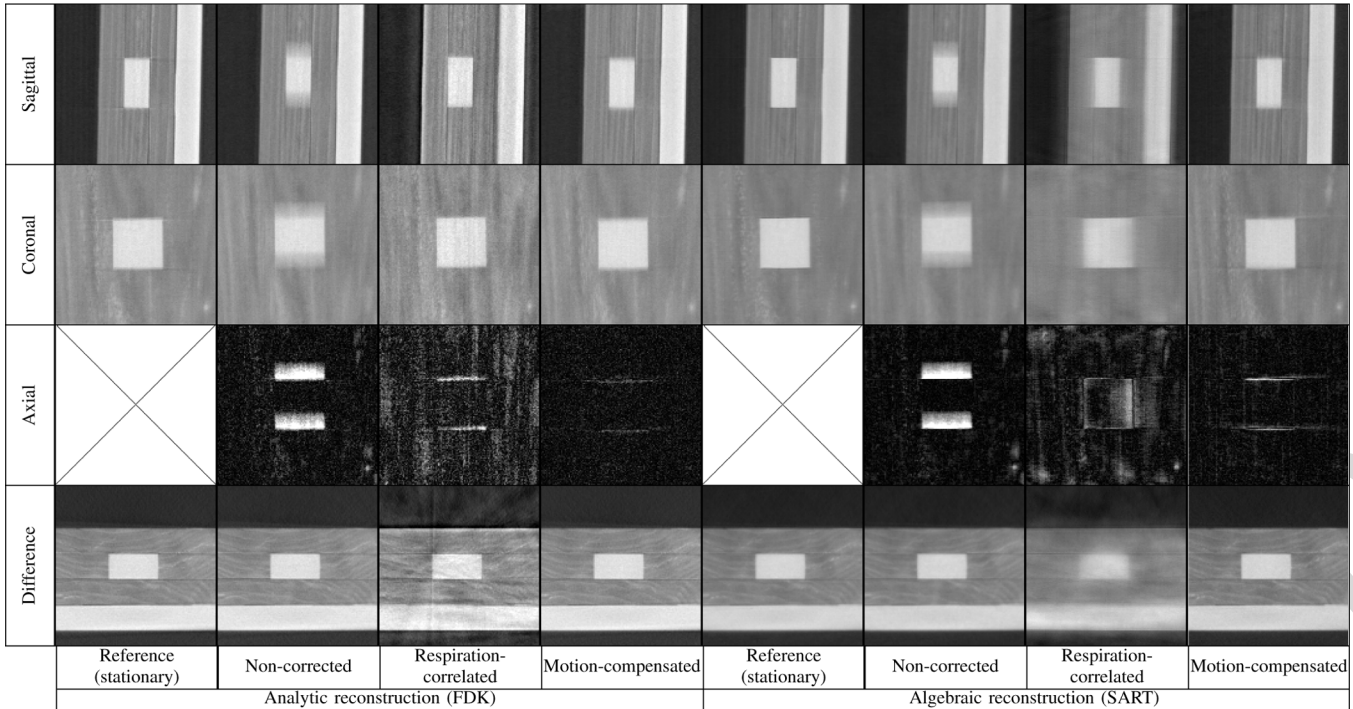


Fig. 14. Real data with a mechanical phantom (Section IV-A3). First, second and fourth rows: slices at the isocenter of the reconstructed CT images. Third row: coronal slice of the absolute difference between each reconstructed CT image and the reference CT scan. The images were cropped to a $128 \times 128 \text{ mm}^2$ size around the isocenter for a better visualization. An identical grey level window was used for all images.

3) *Real Data With a Mechanical Phantom*: A sequence of CB projections was acquired on the CBCT scanner of the Elekta Synergy system (Elekta Oncology Systems Ltd., West Sussex, U.K.) with a phantom placed on a mobile platform. The acquisition parameters were 120 kVp, 10 mA, and 10 ms. The motion of the platform was a sinusoidal translation in the cranio-caudal direction. The peak-to-peak amplitude was 14 mm and the period was 3.5 s. The phantom was composed of a stack of three $20 \times 20 \times 2 \text{ cm}^3$ slabs of wood ($\mu \simeq 0.4 \text{ g} \cdot \text{cm}^{-3}$) with a $4 \times 4 \times 2 \text{ cm}^3$ cube of polyethylene ($\mu = 0.98 \text{ g} \cdot \text{cm}^{-3}$) inserted in the center of the middle slab (Fig. 7).

The respiratory signal was estimated by automatically fitting a sinusoid on the points corresponding to the extreme positions of the platform. The temporal value of these points were selected manually on the sequence of CB projections [Fig. 7(d)]. The maximum translation was measured on the 3-D CT images acquired while the phantom was stationary at the two extreme positions of the platform. Finally, the motion model was obtained by weighting the maximum translation by the respiratory signal value at each acquisition time.

4) *Patient Data*: A sequence of CB projections was acquired on the patient for whom CB projections were simulated (Section IV-A2). The acquisition parameters were 120 kVp, 40 mA, and 25 ms. The diameter of the tumor was approximately 27 mm and its maximum displacement 11 mm.

B. Metrics

We used three metrics to evaluate quantitatively the reconstructed CT images of the phantoms. The first two metrics evaluated the noise induced by the motion and the reconstruction

technique, and the third one estimated the blur. These metrics were applied to a region of interest (ROI) containing the tumor (digital phantoms) or the insert (mechanical phantom) in every position of the phantoms (Fig. 8).

1) *Signal-to-Noise Ratio (SNR)*: The SNR is given by

$$\text{SNR}(\text{dB}) = 20 \log_{10} \frac{\text{RMS}(\text{signal})}{\text{RMS}(\text{noise})} \quad (20)$$

where RMS is the root mean square of voxel intensities, the signal is the expected CT image and the noise is the voxel-to-voxel difference between expected and reconstructed CT images.

2) *Contrast-to-Noise Ratio (CNR)*: The CNR is given by

$$\text{CNR} = \frac{|S_{\text{fg}} - S_{\text{bg}}|}{\sigma_{\text{bg}}} \quad (21)$$

where S_{fg} and S_{bg} are the mean pixel values in the foreground and background, respectively, and σ_{bg} the standard deviation of pixel values in the background. The foreground corresponds to the tumor region segmented in the ROI and the background to the rest of the ROI. The foreground of the ROI was segmented in reference CT images using a manually determined threshold.

3) *Blur Criterion (BC)*: The BC used in this study was proposed by Kriminski *et al.* [5] to quantify the blur independently from the noise. Measures with the BC have arbitrary units and are only comparable relatively to each other on images of a same object, higher values meaning higher blur. Thus, lower BC values mean better results.

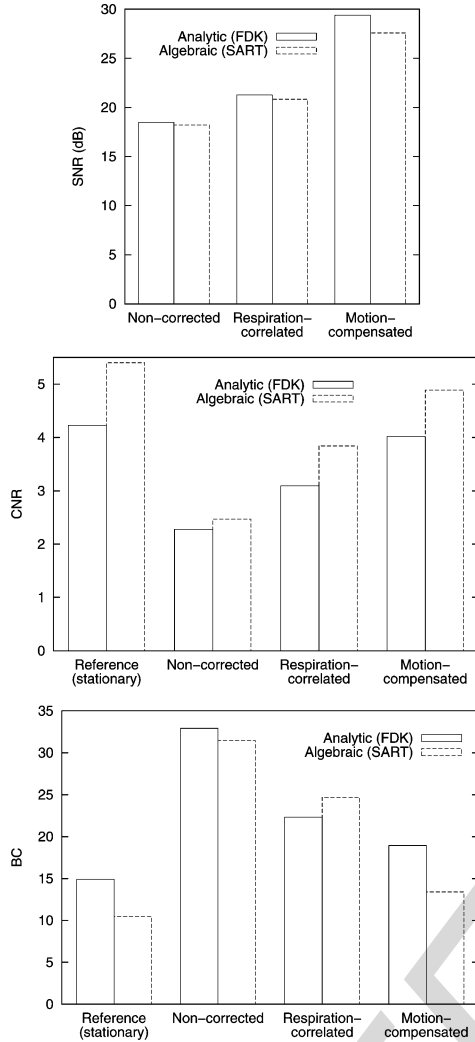


Fig. 15. Real data with a mechanical phantom (Section IV-A3): quantitative analysis of the reconstructed CT images (Fig. 14). The phantom was stationary for the reference image and dynamic for the other results. No reference value is given for the SNR as the reference CT image is used as a signal for SNR computation.

V. RESULTS

A. Reconstructed CT Images

Different CT images were reconstructed for each sequence of CB projections and each reconstruction technique (FDK and SART). The *noncorrected* CT images were reconstructed from all the CB projections using the static algorithm, which corresponds to the reconstruction when the motion is not taken into account. The *respiration-correlated* CT images were reconstructed from a subset of the CB projections using the same static algorithm. This subset was obtained by selecting, for each respiratory cycle, the CB projection closest to the reference position (end-inhale). Finally, the *motion-compensated* CT images were reconstructed from all the CB projections. For comparison, the reference CT images of the phantom were also reconstructed for the phantoms from the sequence of CB projections simulated or acquired with the phantom stationary at the reference position.

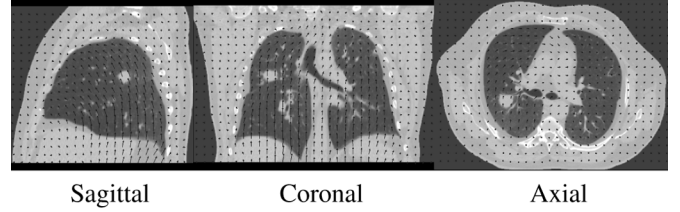


Fig. 16. Zoomed image of estimated motion vectors toward end-exhale superimposed on the slices of the reference CT image (end-inhale) of the 4-D CT image used for the realistic digital phantom and the patient data (Sections IV-A2 and IV-A4).

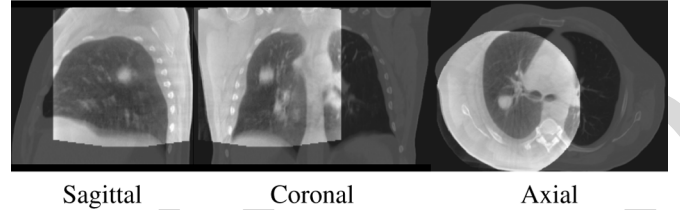


Fig. 17. Complementary color overlay of slices of the blurred 3-D CT image (green), reconstructed from all CB projections of the patient data (Section IV-A4), superimposed after rigid registration on the average 3-D CT image of the 4-D CT image (purple).

The resolution of the CT images was $256 \times 256 \times 256$ voxels of $1 \times 1 \times 1 \text{ mm}^3$ except for the realistic phantom for which it was identical to the resolution of the 3-D CT image used for simulation, i.e., $270 \times 270 \times 133$ voxels of $0.98 \times 0.98 \times 2 \text{ mm}^3$. For algebraic reconstruction, 3 iterations were performed for *static* and *motion-compensated* CT images [53] and 30 iterations for *respiration-correlated* CT images because the number of CB projections is lower.

The slices at the isocenter of the reconstructed CT images are given in Figs. 9, 11, 14, and 18. Profiles in the left-right direction through the tumor are given for the two motion-compensated CT images of the two digital phantoms in Fig. 13. The quantitative evaluation of phantom images is given in Figs. 10, 12, and 15.

B. Motion Estimation From Patient Data

The different components of the motion estimation of the patient were evaluated separately. The deformable registration, applied on the 4-D CT image acquired on a conventional CT scanner, was evaluated based on landmarks identified by medical experts [52], [54]. The mean/standard deviation of the target registration error was 1.2/0.4 mm, with a maximum of 2.6 mm. Fig. 16 illustrates one of the estimated vector fields. The respiratory signal was evaluated by comparing end-exhale and end-inhale temporal positions extracted (1) automatically from the respiratory signal based on changes of the derivative sign and (2) manually via a selection by an expert in the sequence of CB projections [55]. The mean absolute difference was 0.02 s. Finally, the precision of the rigid registration was visually assessed (Fig. 17).

VI. DISCUSSION AND CONCLUSION

Motion-compensated reconstruction allows to obtain CBCT images with a quality close to that obtained for the reconstruc-

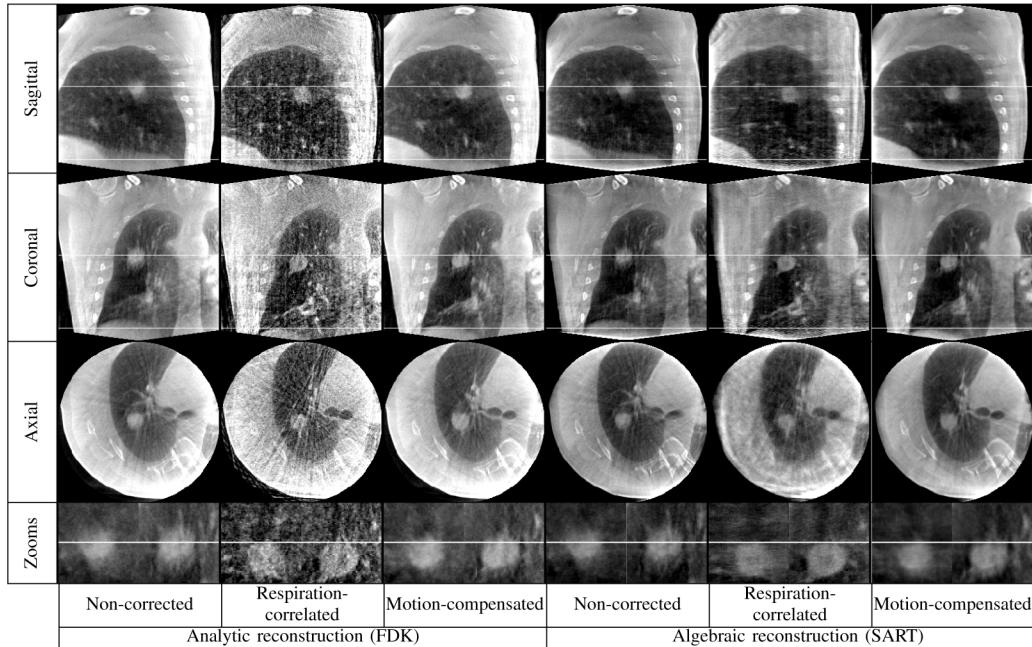


Fig. 18. Patient data (Section IV-A4): slices at the isocenter of the reconstructed CT images with zooms centered on the tumor on sagittal and coronal slices. An identical grey level window was used for all images.

tion of a stationary object using both the analytic (FDK) and the algebraic (SART) methods. The blur is almost fully eliminated and streaks and bands are reduced on the four datasets, both visually (Figs. 9, 11, 13, 14, and 18) and quantitatively on phantom data (Figs. 10, 12, and 15). These methods provide better results than respiration-correlated CBCT. Indeed, respiration-correlated CT involves the selection of only a subset of the CB projections, which causes artifacts due to missing data [4], [7]; these artifacts are mostly streaks and bands when using analytic reconstruction and blur when using algebraic reconstruction.

Numerical phantoms allow comparison between the analytic and the algebraic reconstruction independently from motion estimation because the motion model is then perfectly known. Quantitatively, the metric values are very close to the reference in both cases (Figs. 10 and 12). However, there is a perceptible visual difference between the two methods (Figs. 9, 11, and 13). The analytic reconstruction method, based on a heuristic, does not fully correct the streaks and bands, which is in accordance with Li *et al.* results [21]. Indeed, the analytic algorithm only compensates for the motion locally, in the regions where the motion takes place, while it is known that the motion of a contrasted object implies streak artifacts along the X-rays tangential to the object. These streaks can cross static regions where no compensation is applied. As a consequence, the streaks in motion-compensated CT images can be curved (Fig. 9). On the contrary, the algebraic reconstruction allows full correction of the motion artifacts. This is more visible on the difference images of axial slices where the remaining errors in algebraic reconstruction are mostly due to interpolation. Even though out of the scope of this paper, we note that the impact of truncation also varies with the method used: it causes more artifacts in analytic reconstruction

than in algebraic reconstruction (see reference images in Figs. 9 and 11).

The two reconstruction methods give promising results when applied to the two sequences of real CB projections (mechanical phantom and patient) acquired on the CB scanner but their comparative evaluation is more difficult than when using digital phantoms. First, the motion of the mechanical phantom was limited to a cranio-caudal translation which belongs to the category of deformations that can be exactly compensated [19]. Second, the estimation of patient motion was not precise because it relied on the hypotheses that the motion is regular and identical to the motion of the patient during the acquisition of the 4-D CT image on the conventional CT scanner. Therefore, we observe no visible differences between the two methods, unlike when using digital phantoms: the two motion compensated CT images of the mechanical phantom have a quality similarly close to the reference (Figs. 14 and 15) and both motion-compensated CT images of the patient partially correct the motion artifacts (Fig. 18).

The tissue deformations can imply variations of the linear attenuation of a physical point which were not taken into account in this study (4). For the three phantom datasets, this was because they were either not simulated (digital phantoms) or null (mechanical phantom animated by a rigid motion). However, for the patient dataset, the methods could be improved by characterizing the local variation of volume with the Jacobian of the deformation Φ as proposed by Rey *et al.* [56]: $dV_t \simeq \text{Jac}(\Phi_t) \cdot dV_0$. The local variation of volume can then be linked to the local variation of linear attenuation f by assuming that the linear attenuation is proportional to the mass density and by using the preservation of mass. Many other improvements could be made when operating on real data, such as scatter correction.

TABLE I
COMPUTATIONAL TIMES FOR THE RECONSTRUCTION OF THE IMAGES
OF THE MECHANICAL PHANTOM WITH AN IDENTICAL 256^3
VOXELS OF 1 mm^3 FIELD-OF-VIEW, I.E., NO CORRECTION
OF THE TRUNCATION IN ALGEBRAIC RECONSTRUCTION

Method	Reconstruction times	
	Analytic	Algebraic
Non-corrected	18 min	165 min
Motion-compensated	28 min	392 min

The computational time was not a major concern of this work but it is still interesting to observe the relative differences (Table I). With the analytic methods, motion-compensated reconstruction took 56% more time than uncompensated reconstruction; with the algebraic methods, the difference amounted to 138%. The two kinds of methods are not really comparable because a larger field of view is necessary to correct for the truncation when using algebraic reconstruction. But even when the same field-of-view was used, the motion-compensated reconstruction was 14 times longer with the algebraic method than with the analytic method. This is due to the algorithm complexity which is six times greater with algebraic reconstruction, due to the three projections and backprojections required per CB projection (one per iteration), than with analytic reconstruction which only involves one backprojection per CB projection. Moreover, the projection involves more computation than the backprojection.

Two cases can be sketched for clinical implementation. In the first case, the CBCT image is used just after the acquisition to estimate the patient's position. The estimation of the motion model from the 4-D CT image acquired on a conventional scanner could be done before the CB acquisition. As soon as an estimate of the spatial rigid registration is available, the motion-compensated CBCT image can be reconstructed on-the-fly using the analytic method to be available a few seconds after the end of the acquisition [57]. In the second case, the CBCT image is used after the delivery of the treatment fraction for adaptive radiation therapy [58]. Either of the proposed methods, analytic or algebraic, could then be used.

This study focused on the reconstruction aspects of motion-compensated CBCT. As estimating the respiratory motion is a prior to reconstruction, we proposed to prove the concepts on patient data by supposing that the respiratory motion was regular during the acquisition and similar to the one represented by the 4-D CT image acquired on a conventional scanner. Results obtained here on real patient data as well as another study on more patients [57] suggest that even a rough estimation can correct most motion artifacts but further validation based on more patient images is required to assess the robustness of the method to inaccuracies of the estimated motion. If necessary, the estimation could be improved with more sophisticated methods [14] which could use low quality reconstructed CBCT images to refine the motion estimation [59]. However, validation will be a major concern, as is the case with all nonrigid registration methods because no gold standard is available for patient data.

This study compared the quality of CBCT images reconstructed with analytic and algebraic methods. Motion-compensated algebraic reconstruction gave near perfect results when the motion was known whereas streak artifacts remained when

using analytic reconstruction (Figs. 9, 11, and 13). Future works will focus on motion estimation, which requires validation using an anthropomorphic phantom [60] and more patient images along with statistical analysis.

ACKNOWLEDGMENT

The authors would like to thank Prof. M. van Herk for critical reading and for permitting the use of the viewer developed at The Netherlands Cancer Institute.

REFERENCES

- [1] D. A. Jaffray, J. H. Siewerdsen, J. W. Wong, and A. A. Martinez, "Flat-panel cone-beam computed tomography for image-guided radiation therapy," *Int. J. Radiat. Oncol. Biol. Phys.*, vol. 53, no. 5, pp. 1337–1349, 2002.
- [2] C. J. Ritchie, J. D. Godwin, C. R. Crawford, W. Stanford, H. Anno, and Y. Kim, "Minimum scan speeds for suppression of motion artifacts in CT," *Radiology*, vol. 185, no. 1, pp. 37–42, 1992.
- [3] G. T. Y. Chen, J. H. Kung, and K. P. Beaudette, "Artifacts in computed tomography scanning of moving objects," *Semin. Radiat. Oncol.*, vol. 14, no. 1, pp. 19–26, 2004.
- [4] J.-J. Sonke, L. Zijp, P. Remeijer, and M. van Herk, "Respiratory correlated cone beam CT," *Med. Phys.*, vol. 32, no. 4, pp. 1176–1186, 2005.
- [5] S. Kriminski, M. Mitschke, S. Sorensen, N. M. Wink, P. E. Chow, S. Tenn, and T. D. Solberg, "Respiratory correlated cone-beam computed tomography on an isocentric C-arm," *Phys. Med. Biol.*, vol. 50, no. 22, pp. 5263–5280, 2005.
- [6] L. Dietrich, S. Jetter, T. Tücking, S. Nill, and U. Oelfke, "Linac-integrated 4-D cone beam CT: First experimental results," *Phys. Med. Biol.*, vol. 51, no. 11, pp. 2939–2952, 2006.
- [7] T. Li, L. Xing, P. Munro, C. McGuinness, M. Chao, Y. Yang, B. Loo, and A. Koong, "Four-dimensional cone-beam computed tomography using an on-board imager," *Med. Phys.*, vol. 33, no. 10, pp. 3825–3833, 2006.
- [8] M. van Herk, L. Zijp, P. Remeijer, J. Wolthaus, and J.-J. Sonke, "On-line 4-D cone beam CT for daily correction of lung tumour position during hypofractionated radiotherapy," in *Int. Conf. Use Comput. Radiation Therapy (ICCR)*, Toronto, ON, Canada, 2007.
- [9] S. Rit, D. Sarrut, and S. Miguet, "Gated cone-beam CT imaging of the thorax: A reconstruction study," in *SPIE Med. Imag.*, San Diego, CA, 2007, vol. 6510, p. 651022.
- [10] D. Sarrut, V. Boldea, S. Miguet, and C. Ginestet, "Simulation of four-dimensional CT images from deformable registration between inhale and exhale breath-hold CT scans," *Med. Phys.*, vol. 33, no. 3, pp. 605–617, 2006.
- [11] C. Blondel, R. Vaillant, G. Malandain, and N. Ayache, "3-D tomographic reconstruction of coronary arteries using a precomputed 4-D motion field," *Phys. Med. Biol.*, vol. 49, no. 11, pp. 2197–2208, 2004.
- [12] C. Blondel, G. Malandain, R. Vaillant, and N. Ayache, "Reconstruction of coronary arteries from a single rotational X-ray projection sequence," *IEEE Trans. Med. Imag.*, vol. 25, no. 5, pp. 653–663, May 2006.
- [13] R. Zeng, J. A. Fessler, and J. M. Balter, "Respiratory motion estimation from slowly rotating X-ray projections: Theory and simulation," *Med. Phys.*, vol. 32, no. 4, pp. 984–991, 2005.
- [14] R. Zeng, J. A. Fessler, and J. M. Balter, "Estimating 3-D respiratory motion from orbiting views by tomographic image registration," *IEEE Trans. Med. Imag.*, vol. 26, no. 2, pp. 153–163, Feb. 2007.
- [15] A. Schweikard, H. Shiomi, and J. Adler, "Respiration tracking in radio-surgery without fiducials," *Int. J. Med. Robot.*, vol. 1, no. 2, pp. 19–27, 2005.
- [16] M. Reyes, G. Malandain, P. M. Koulibaly, M. A. González-Ballester, and J. Darcourt, "Model-based respiratory motion compensation for emission tomography image reconstruction," *Phys. Med. Biol.*, vol. 52, no. 12, pp. 3579–3600, 2007.
- [17] C. R. Crawford, K. F. King, C. J. Ritchie, and J. D. Godwin, "Respiratory compensation in projection imaging using a magnification and displacement model," *IEEE Trans. Med. Imag.*, vol. 15, no. 3, pp. 327–332, Jun. 1996.
- [18] S. Roux, L. Desbat, A. Koenig, and P. Grangeat, "Exact reconstruction in 2-D dynamic CT: Compensation of time-dependent affine deformations," *Phys. Med. Biol.*, vol. 49, no. 11, pp. 2169–2182, 2004.

- [19] L. Desbat, S. Roux, and P. Grangeat, "Compensation of some time dependent deformations in tomography," *IEEE Trans. Med. Imag.*, vol. 26, no. 2, pp. 261–269, Feb. 2007.
- [20] P. Grangeat, A. Koenig, T. Rodet, and S. Bonnet, "Theoretical framework for a dynamic cone-beam reconstruction algorithm based on a dynamic particle model," *Phys. Med. Biol.*, vol. 47, no. 15, pp. 2611–2625, 2002.
- [21] T. Li, E. Schreibmann, Y. Yang, and L. Xing, "Motion correction for improved target localization with on-board cone-beam computed tomography," *Phys. Med. Biol.*, vol. 51, no. 2, pp. 253–267, 2006.
- [22] C. J. Ritchie, C. R. Crawford, J. D. Godwin, K. F. King, and Y. Kim, "Correction of computed tomography motion artifacts using pixel-specific back-projection," *IEEE Trans. Med. Imag.*, vol. 15, no. 3, pp. 333–342, Jun. 1996.
- [23] K. Taguchi and H. Kudo, "Motion compensated fan-beam reconstruction for nonrigid transformation," *IEEE Trans. Med. Imag.*, vol. 27, no. 7, pp. 907–917, Jul. 2008.
- [24] L. A. Feldkamp, L. C. Davis, and J. W. Kress, "Practical cone-beam algorithm," *J. Opt. Soc. Am. A*, vol. 1, no. 6, pp. 612–619, 1984.
- [25] B. Ohnesorge, T. Flohr, K. Schwarz, J. P. Heiken, and K. T. Bae, "Efficient correction for CT image artifacts caused by objects extending outside the scan field of view," *Med. Phys.*, vol. 27, no. 1, pp. 39–46, 2000.
- [26] A. H. Andersen and A. C. Kak, "Simultaneous algebraic reconstruction technique (SART): A superior implementation of the art algorithm," *Ultrason. Imag.*, vol. 6, no. 1, pp. 81–94, 1984.
- [27] R. Gordon, R. Bender, and G. T. Herman, "Algebraic reconstruction techniques (ART) for three-dimensional electron microscopy and X-ray photography," *J. Theor. Biol.*, vol. 29, no. 3, pp. 471–481, 1970.
- [28] M. Jiang and G. Wang, "Convergence of the simultaneous algebraic reconstruction technique (SART)," *IEEE Trans. Image Process.*, vol. 12, no. 8, pp. 957–961, Aug. 2003.
- [29] K. Mueller, R. Yagel, and J. F. Cornhill, "The weighted-distance scheme: A globally optimizing projection ordering method for ART," *IEEE Trans. Med. Imag.*, vol. 16, no. 2, pp. 223–230, Apr. 1997.
- [30] P. M. Joseph, "An improved algorithm for reprojecting rays through pixel images," *IEEE Trans. Med. Imag.*, vol. 1, no. 3, pp. 192–196, Nov. 1982.
- [31] B. De Man and S. Basu, "Distance-driven projection and backprojection in three dimensions," *Phys. Med. Biol.*, vol. 49, no. 11, pp. 2463–2475, 2004.
- [32] F. Xu and K. Mueller, "A comparative study of popular interpolation and integration methods for use in computed tomography," in *IEEE Int. Symp. Biomed. Imag. (ISBI)*, Apr. 2006, pp. 1252–1255.
- [33] R. L. Siddon, "Fast calculation of the exact radiological path for a three-dimensional CT array," *Med. Phys.*, vol. 12, no. 2, pp. 252–255, 1985.
- [34] P. G. Lacroute, "Fast volume rendering using a shear-warp factorization of the viewing transformation" Ph.D. dissertation, Stanford Univ., Stanford, CA, 1995 [Online]. Available: http://www-graphics.stanford.edu/papers/lacroute_thesis/
- [35] C. Riddell and Y. Trousset, "Rectification for cone-beam projection and backprojection," *IEEE Trans. Med. Imag.*, vol. 25, no. 7, pp. 950–962, Jul. 2006.
- [36] H. Kunze, K. Stierstorfer, and W. Härer, "Pre-processing of projections for iterative reconstruction," in *Fully 3-D Image Reconstruction Radiol. Nucl. Med. Conf.*, Salt Lake City, UT, 2005, pp. 84–87.
- [37] W. Zbijewski and F. J. Beekman, "Comparison of methods for suppressing edge and aliasing artefacts in iterative X-ray CT reconstruction," *Phys. Med. Biol.*, vol. 51, no. 7, pp. 1877–1889, 2006.
- [38] M. Jiang and G. Wang, "Convergence studies on iterative algorithms for image reconstruction," *IEEE Trans. Med. Imag.*, vol. 22, no. 5, pp. 569–579, May 2003.
- [39] B. Zhang and G. L. Zeng, "Two-dimensional iterative region-of-interest (ROI) reconstruction from truncated projection data," *Med. Phys.*, vol. 34, no. 3, pp. 935–944, 2007.
- [40] F. Lamare, T. Cresson, J. Savean, C. Cheze Le Rest, A. J. Reader, and D. Visvikis, "Respiratory motion correction for PET oncology applications using affine transformation of list mode data," *Phys. Med. Biol.*, vol. 52, no. 1, pp. 121–140, 2007.
- [41] S. Rit and D. Sarrut, "Cone-beam projection of a deformable volume for motion compensated algebraic reconstruction," in *Conf. Proc. IEEE Eng. Med. Biol. Soc.*, Lyon, France, 2007, vol. 2007, pp. 6544–6547.
- [42] G. Wolberg, *Digital Image Warping*. Los Alamitos, CA: IEEE Computer Soc. Press, 1990.
- [43] V. Boldea, D. Sarrut, and S. Clippe, "Lung deformation estimation with non-rigid registration for radiotherapy treatment," in *Medical Image Computing and Computer-Assisted Intervention (MICCAI)*, Montréal, QC, Canada, 2003, vol. 2878, pp. 770–777.
- [44] V. Boldea, G. C. Sharp, S. B. Jiang, and D. Sarrut, "4-D-CT lung motion estimation with deformable registration: Quantification of motion nonlinearity and hysteresis," *Med. Phys.*, vol. 35, no. 3, pp. 1008–1018, 2008.
- [45] Y. Seppenwoolde, H. Shirato, K. Kitamura, S. Shimizu, M. van Herk, J. V. Lebesque, and K. Miyasaka, "Precise and real-time measurement of 3-D tumor motion in lung due to breathing and heartbeat, measured during radiotherapy," *Int. J. Radiat. Oncol. Biol. Phys.*, vol. 53, no. 4, pp. 822–834, 2002.
- [46] V. Boldea, "Intégration de la Respiration en Radiothérapie : Apport du Recalage Déformable D'images" Ph.D. Dissertation, Univ. Lumière Lyon 2, Lyon, 2006 [Online]. Available: <http://liris.cnrs.fr/publis/?id=2959>
- [47] J.-J. Sonke, J. Lebesque, and M. van Herk, "Variability of four-dimensional computed tomography patient models," *Int. J. Radiat. Oncol. Biol. Phys.*, vol. 70, no. 2, pp. 590–598, 2008.
- [48] G. D. Hugo, J. Liang, J. Campbell, and D. Yan, "On-line target position localization in the presence of respiration: A comparison of two methods," *Int. J. Radiat. Oncol. Biol. Phys.*, vol. 69, no. 5, pp. 1634–1641, 2007.
- [49] J. Vandemeulebroucke, E. Vansteenkiste, and W. Philips, "A multi-modal 2-D/3-D registration scheme for preterm brain images," in *Conf. Proc. IEEE Eng. Med. Biol. Soc.*, 2006, vol. 1, pp. 3341–3344.
- [50] S. Rit, D. Sarrut, and C. Ginestet, "Respiratory signal extraction for 4-D CT imaging of the thorax from cone-beam CT projections," in *Medical Image Computing and Computer-Assisted Intervention (MICCAI)*, Palm Springs, 2005, vol. 3749, pp. 556–563.
- [51] A. E. Lujan, E. W. Larsen, J. M. Balter, and R. K. Ten Haken, "A method for incorporating organ motion due to breathing into 3-D dose calculations," *Med. Phys.*, vol. 26, no. 5, pp. 715–720, 1999.
- [52] J. Vandemeulebroucke, D. Sarrut, and P. Clarysse, "Point-validated pixel-based breathing thorax model," in *Int. Conf. Use Computers Radiation Therapy (ICCR)*, Toronto, ON, Canada, 2007 [Online]. Available: <http://www.creatis.insa-lyon.fr/rio/popi-model>
- [53] K. Mueller, R. Yagel, and J. J. Wheller, "Anti-aliased three-dimensional cone-beam reconstruction of low-contrast objects with algebraic methods," *IEEE Trans. Med. Imag.*, vol. 18, no. 6, pp. 519–537, Jun. 1999.
- [54] D. Sarrut, B. Delhay, P.-F. Villard, V. Boldea, M. Beuve, and P. Clarysse, "A comparison framework for breathing motion estimation methods from 4-D imaging," *IEEE Trans. Med. Imag.*, vol. 26, no. 12, pp. 1636–1648, Dec. 2007.
- [55] S. Rit, "Prise en Compte du Mouvement Respiratoire Pour la Reconstruction D'images Tomodensitométriques" Ph.D. dissertation, Univ. Lumière Lyon 2, Lyon, France, 2007 [Online]. Available: <http://liris.cnrs.fr/publis/?id=3354>
- [56] D. Rey, G. Subsol, H. Delingette, and N. Ayache, "Automatic detection and segmentation of evolving processes in 3-D medical images: Application to multiple sclerosis," *Med. Image Anal.*, vol. 6, no. 2, pp. 163–179, 2002.
- [57] S. Rit, J. Wolthaus, M. van Herk, and J.-J. Sonke, "On-the-fly motion-compensated cone-beam CT using an a priori motion model," in *Medical Image Computing and Computer-Assisted Intervention (MICCAI)*, New York, 2008, vol. 5241, pp. 729–736.
- [58] D. Yan, F. Vicini, J. Wong, and A. Martinez, "Adaptive radiation therapy," *Phys. Med. Biol.*, vol. 42, no. 1, pp. 123–132, 1997.
- [59] T. Li, A. Koong, and L. Xing, "Enhanced 4-D cone-beam CT with inter-phase motion model," *Med. Phys.*, vol. 34, no. 9, pp. 3688–3695, 2007.
- [60] R. Lin, E. Wilson, J. Tang, D. Stoianovici, and K. Cleary, "A computer-controlled pump and realistic, anthropomorphic respiratory phantom for validating image-guided systems," in *SPIE Med. Imag.*, 2007, vol. 6510 [AUTHOR: PAGES?].